











Article

Monitoring Effect of Spatial Growth on Land Surface Temperature in Dhaka

Md. Mustafizur Rahman ¹, Ram Avtar ^{1,2,*}, Ali P. Yunus ³, Jie Dou ⁴, Prakhar Misra ⁵,
Wataru Takeuchi ⁵, Netrananda Sahu ^{6,7}, Pankaj Kumar ⁸, Brian Alan Johnson ⁸,
Rajarshi Dasgupta ⁸, Ali Kharrazi ^{9,10,11}, Shamik Chakraborty ¹² and
Tonni Agustiono Kurniawan ¹³

¹ Graduate School of Environmental Science, Hokkaido University, Sapporo, Hokkaido 060-0810, Japan; rahman870_hu@eis.hokudai.ac.jp

² Faculty of Environmental Earth Science, Hokkaido University, Sapporo, Hokkaido 060-0810, Japan

³ State Key Laboratory of Geohazard Prevention and Geoenvironment Protection, Chengdu University of Technology, Chengdu 610059, China; yunusp@csis.u-tokyo.ac.jp

⁴ Department of Civil and Environmental Engineering, Nagaoka University of Technology, Nagaoka, Niigata 940-2188, Japan; douj888@vos.nagaokaut.ac.jp

⁵ Institute of Industrial Science, The University of Tokyo, Tokyo 153-8505, Japan; mprakhar@iis.u-tokyo.ac.jp (P.M.); wataru@iis.u-tokyo.ac.jp (W.T.)

⁶ Department of Geography, Delhi School of Economics, University of Delhi, New Delhi 110007, India; nsahu@geography.du.ac.in

⁷ Disaster Prevention Research Institute, Kyoto University, Kyoto 611-0011, Japan

⁸ Natural Resources and Ecosystem Services, Institute for Global Environmental Strategies, Hayama 240-0115, Japan; kumar@iges.or.jp (P.K.); johnson@iges.or.jp (B.A.J.); dasgupta@iges.or.jp (R.D.)

⁹ Advanced Systems Analysis Group, International Institute for Applied Systems Analysis, Schlossplatz 1, A-2361 Laxenburg, Austria; kharrazi@iiasa.ac.at

¹⁰ Faculty of International Liberal Arts Global Studies Program, Akita International University, Yuwa City, Akita 010-1292, Japan

¹¹ CMCC Foundation – Euro-Mediterranean Center on Climate Change and Ca' Foscari University of Venice, 30175 Venice, Italy

¹² Faculty of Sustainability Studies, Hosei University, 2-17-2 Fujimi, Chiyoda-ku, Tokyo 102-8160, Japan; shamik.chakraborty.76@hosei.ac.jp

¹³ Key Laboratory of the Coastal and Wetland Ecosystems (Xiamen University), Ministry of Education, College of the Environment and Ecology, Xiamen University, Xiamen 361102, China; tonni@xmu.edu.cn

* Correspondence: ram@ees.hokudai.ac.jp; Tel.: +81-011-706-2261

Received: 7 March 2020; Accepted: 4 April 2020; Published: 8 April 2020



Abstract: Spatial urban growth and its impact on land surface temperature (LST) is a high priority environmental issue for urban policy. Although the impact of horizontal spatial growth of cities on LST is well studied, the impact of the vertical spatial distribution of buildings on LST is under-investigated. This is particularly true for cities in sub-tropical developing countries. In this study, TerraSAR-X add-on for Digital Elevation Measurement (TanDEM-XDEM), Advanced Spaceborne Thermal Emission and Reflection (ASTER)-Global Digital Elevation Model (GDEM), and ALOS World 3D-30m (AW3D30) based Digital Surface Model (DSM) data were used to investigate the vertical growth of the Dhaka Metropolitan Area (DMA) in Bangladesh. Thermal Infrared (TIR) data (10.6–11.2 μ m) of Landsat-8 were used to investigate the seasonal variations in LST. Thereafter, the impact of horizontal and vertical spatial growth on LST was studied. The result showed that: (a) TanDEM-X DSM derived building height had a higher accuracy as compared to other existing DSM that reveals mean building height of the Dhaka city is approximately 10 m, (b) built-up areas were estimated to cover approximately 94%, 88%, and 44% in Dhaka South City Corporation (DSCC), Dhaka North City Corporation (DNCC), and Fringe areas, respectively, of DMA using a Support Vector Machine (SVM) classification method, (c) the built-up showed a strong relationship with LST (Kendall tau coefficient of 0.625 in summer

and 0.483 in winter) in comparison to vertical growth (Kendall tau coefficient of 0.156 in the summer and 0.059 in the winter), and (d) the 'low height-high density' areas showed high LST in both seasons. This study suggests that vertical development is better than horizontal development for providing enough open spaces, green spaces, and preserving natural features. This study provides city planners with a better understating of sustainable urban planning and can promote the formulation of action plans for appropriate urban development policies.

Keywords: spatial growth; LST; TanDEM-X -DSM; building height; urban planning

1. Introduction

Unplanned spatial growth of cities is a major cause of increasing land surface temperatures (LST) and the development of urban heat islands (UHI) [1]. Wong and Yu [2] reported that the highest concentration of hard surfaces such as buildings, roads, impervious areas, and fewer open spaces are the reasons for increasing urban surface temperature. Apart from that, the important causes of the urban heat island effect include canyon geometry, thermal properties of materials, anthropogenic heat, the urban greenhouse effect, and evaporation [3–5]. Spatial growth denotes a tremendous increase in population and buildings in cities, which leads to the drastic reduction of vegetated areas while also leading to an increase of impervious areas [6]. According to Cuberers D. [7], the spatial growth of a city refers to both horizontal (the addition of new settlement areas from the core city center to peripheral areas with a modest vertical profile) and vertical (high population density, economic agglomeration, and high building floor-area ratios) urban expansion. The physical growth of cities brings numerous environmental problems, among them being the "urban heat island" effect, which is a well-documented climatological effect of human activities on the urban environment [2,8].

Recently, remotely sensed data such as ASTER, AW3D, TanDEM-X, and Shuttle Radar Topography Mission (SRTM) have emerged in urban studies due to the requirements of quick and extensive spatial information on urban growth. Moreover, remote sensing datasets, for example, the Landsat, Moderate Resolution Imaging Spectroradiometer (MODIS), and ASTER emissivity dataset, are widely used for land surface temperature studies and for taking decisions for the well-being of city dwellers. Remote sensing techniques provide data over large areas along with updated spatial information in a cost-effective way. This makes it easy to study the complex relationship between spatial parameters and thermal conditions [5,9–11]. Remotely sensed data have been widely used in the field of urban planning especially for decision-making and monitoring environmental parameters. For example, vegetation, land surface temperature (LST), built-up area indices, land use/land cover, urban expansion, and hazard mapping have been well documented by many studies [12–15]. Remotely sensed data can also be used for highly accurate 3D surface model extraction in urban areas [16–18]. Misra et al., 2018 [19], used multi-directional processing and slope-dependent filtering approaches to extract digital building heights using Digital Surface Model (DSM) data. They have determined the methodology for DSM-based building height extraction that can be further utilized to study vertical growth and urban compactness, while observing heat islands, flood hazard zonation, monitoring city growth, and thermal energy absorption. A literature review shows that dense areas have fewer open spaces and more built-up areas, and experience a high surface temperature [20–22]. Moreover, solar radiation trapped with multiple reflections of radiation within the 3D geometry increases the urban temperature [23–25]. Land surface temperature is higher in the core urban areas than in the rural areas [26–29]. Another study revealed that the encroachment of wetlands leads to increased surface temperature in the surrounding areas of Kerala, India [30].

Most of the previous studies in urban science focused on the application of remote sensing techniques to monitor change in vegetation cover and impacts on land surface temperature (LST), 3D modeling for vertical growth assessment, urban area expansion, and impacts on land surface

temperatures [19,31–34]. In addition, a study of the suburbs Colorado, USA, explored the characteristics of LST on landscape patterns and vertical structures employing Light Detection and Ranging (LiDAR) data [35]. However, there is no inclusive study that considers LST, building height, and built-up density using cost-effective remote sensing data considering the affordability of developing countries [19,26,35–39]. The use of LiDAR data or laser scanning can provide accurate information about building heights, but it is expensive and not affordable for developing countries. The study presented in this paper is required for the quick and proficient implementation of urban planning policies, especially for rapidly growing cities in developing countries. There is a considerable research gap to integrate two dimensional (2D) and three dimensional (3D) spatial growth and its impacts on LST in the Dhaka Metropolitan Area (DMA) with a focus on urban planning.

In light of the above-mentioned research gap, this study investigates the application of remote sensing in monitoring the impact of urban heat and spatial growth. First, this study offers a glimpse of the current scenario of the spatial growth of DMA, which highlights the building height estimation approach using space-borne sensor data from TanDEM-X, ASTER-GDEM, and AW3D30. Second, this study explores the seasonal variation of LST using Landsat 8 data. Lastly, it emphasizes the relationship between building height, built-up density, and LST, which will form the basis of future guidelines for urban planning and policy implications to create a better living environment.

2. Study Area

Dhaka, which is the capital city of Bangladesh, is one of the largest and most populated cities in the world with a population of 18.89 million people in Greater Dhaka City [40]. To meet the demands of the huge population, the city is growing rapidly both vertically and horizontally. As explained previously in the literature, this spatial growth has adverse impacts on LST as well as microclimatic changes in the city area. Figure 1 depicts the location of the study area, i.e., Dhaka Metropolitan Area (DMA). The DMA lies between 23°41′46.22″N to 23°53′6.3″N latitude and 90°24′9.34″E to 90°24′6.17″E longitude. The DMA includes two City Corporations, namely Dhaka South City Corporation (DSCC with 57 wards) and Dhaka North City Corporation (DNCC with 36 wards) along with the fringe area with 17 unions. DSCC and DNCC are characterized by congested buildings with less open areas. The fringe area is developed by transforming agriculture land to bare land and development of the built-up area. Figure 2 demonstrates the photographs captured in different zones of DMA. Restricted areas such as Dhaka Cantonment and airport area were excluded from this research. The urbanization rate of DMA is about 4.3%, which leads to encroachment of urban green spaces and wetlands [19]. The climate of Bangladesh is subtropical in the center-north and tropical in the south with a pleasantly warm and sunny winter from November to February. There are four distinct seasons that can be observed in Bangladesh from the climatic point of view: (1) the dry winter season from December to February, (2) the pre-monsoon hot summer season from March to May, (3) the rainy monsoon season from June to September, and (4) the post-monsoon autumn season from October to November [41]. Figure 3 illustrates the monthly average rainfall and temperature pattern of Dhaka city from 2005–2015. The annual average temperature is about 25 °C (77 °F) and the average annual rainfall is about 1300 mm [42]. About 44% area of DMA consists of higher temperature zones (27 °C to <30 °C) and is increasing by 0.32 °C per decade [39].

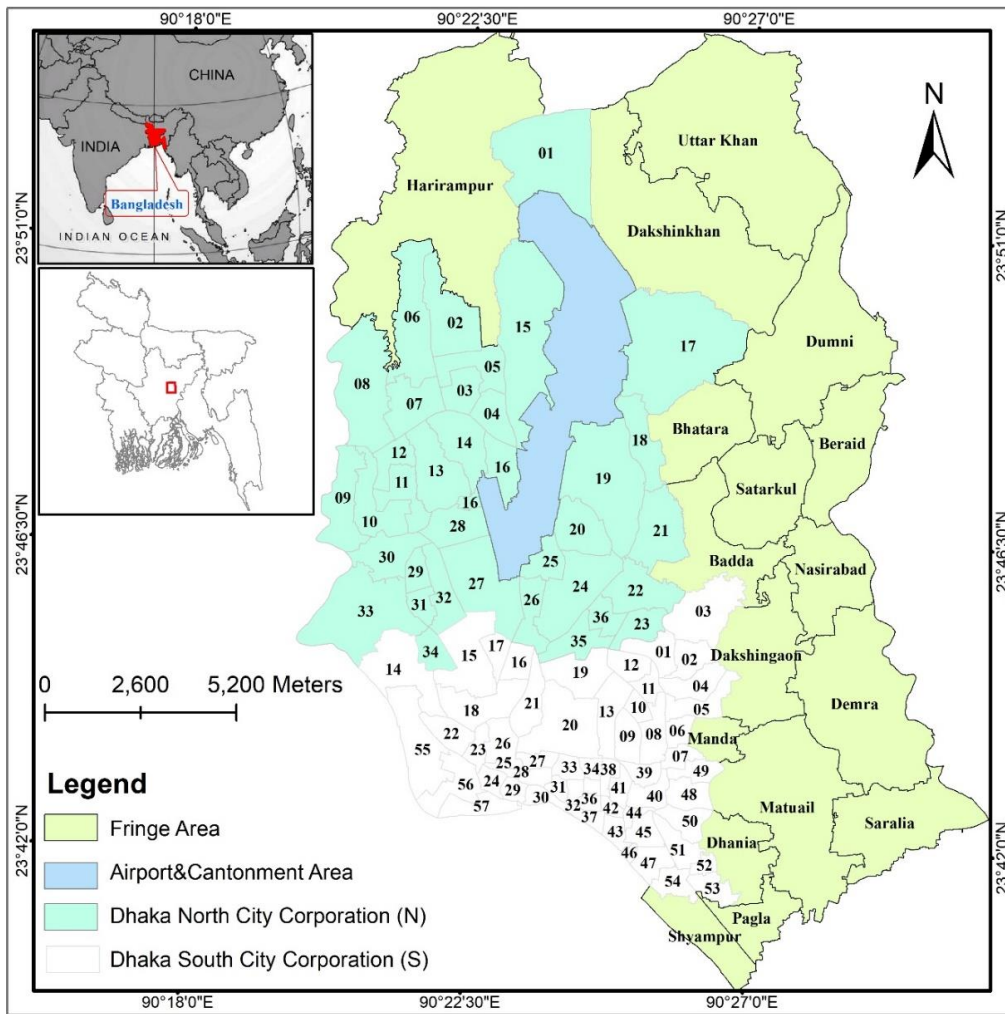


Figure 1. Location of Dhaka Metropolitan Area (DMA) with the distribution of the North City Corporation, South City Corporation, and Fringe areas. Sources: Bangladesh Bureau of Statistics (BBS), 2011, and Capital Development Authority (RAJUK), Dhaka, 2018.



Figure 2. (a) Highly dense built-up area and informal settlement in the Dhaka South City Corporation (DSCC), (b) relatively less congested buildings and formal settlement in the Dhaka North City Corporation (DNCC), (c) built-up area with vegetation in the fringe area, and (d) sand filling for land development in the fringe area.

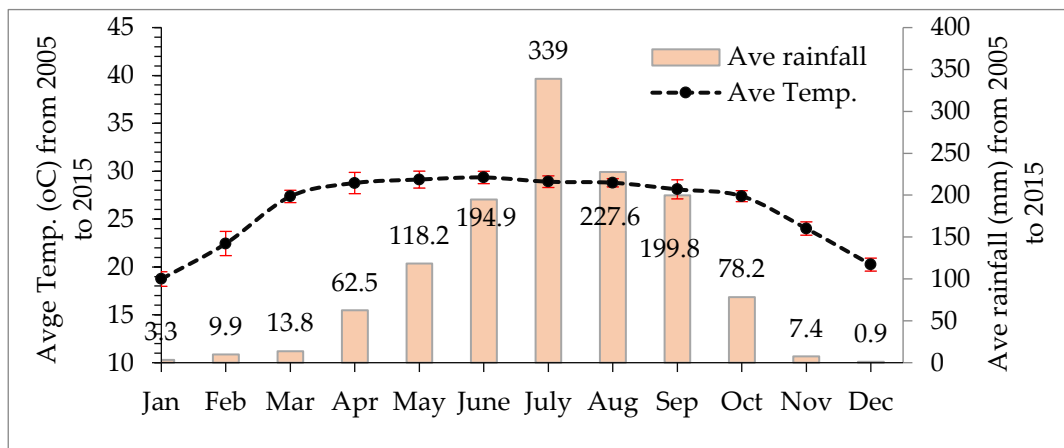


Figure 3. Monthly average temperature and rainfall of Dhaka city (2005 to 2015). Data source: Bangladesh Meteorological Department (2015).

Raja [43] reported that the main causes of urban heat island and microclimatic variations in Dhaka city are dwindling green covers, open spaces, and wetlands along with changes in urban morphology, which increases anthropogenic heat generation, building density, impervious surfaces, and dark-colored rooftops. Ferdous [16] revealed that the uncontrolled urban growth in the DMA leads to an increase in LST because of a decrease in open spaces and water bodies. The objective of this study is to provide policymakers information related to several measures of urban growth and their impact on LST and the microclimate of DMA.

3. Materials and Methods

3.1. Data Sets

Several satellites and ground-based datasets related to LST, build-up, and 3D surface elevation were collected and analyzed in this study. Table 1 represents the summary of various DEMs data and their specification used in this study. DEMs data were useful for extracting building height information. Table 2 illustrates the acquisition of Landsat-8 data and their properties in the study area.

Table 1. Summary of DSMs used in this research. TanDEM-X: (TerraSAR-X Add-On for Digital Elevation Measurements), ASTER GDEM: (Advanced Spaceborne Thermal Emission and Reflection Radiometer), AW3D: (ALOS WORLD 3D).

Data	Acquisition	Vertical Accuracy *	Imaging System	Resolution (m)	Sources
TanDEM-X	16 October 2012	1.6–6.2 m	SAR X band	12	German Aerospace Center, DLR
ASTER (GDEM V2), publicly released 2011	2009	15.1–23.2 m	Optical	30	US Geological Survey (USGS),
AW3D30 Publicly released by JAXA in 2015	2006–2011	1.7–6.8 m	Optical	30	Japan Aerospace Exploration Agency (JAXA)

* Vertical accuracy of the Digital Surface Model (DSM) reported by other studies.

Table 2. Summary of Landsat-8 Operational Land Imager (OLI) used in this research.

Path/Tiles	Acquisition Date	Local Acquisition Time (am)	Band	Source	Remarks
Landsat-8 OLI WRS-2, 137/44	06-11-13	10:26:34.15	Band (3,4,5,6) 30m and TIR band (10,11) 100m	US Geological Survey (USGS),	TIR band for LST retrieval and other bands for Land Use Land Cover (LULC) mapping
	24-12-13	10:26:16.33			
	25-01-14	10:25:56.73			
	06-02-14	10:25:31.49			
	14-03-14	10:25:20.51			
	24-04-14	10:25:51.49			
	06-05-14	10:26:01.49			

3.1.1. TanDEM-X

The TanDEM-X system is a space-borne radar satellite system developed by the German Aerospace Center (DLR) (<https://tandemx-science.dlr.de/>). It is based on two TerraSAR-X radar satellites flying in close formation and equipped with a synthetic aperture radar operating at X-band to generate World DEM [44]. The carrier frequency of the X-band radar is 9.6 GHz (3.1 cm in wavelength) with horizontal-horizontal (HH) polarization at 35.33 degrees of the incidence angle. The range and azimuth pixel spacing are approximately 0.91 m and 1.90 m, respectively [45]. Due to the bi-static mode of data collection, both satellite orbits can acquire data at the same location and at almost the same time with a short baseline [46]. Wessel et al. [47] reported the absolute vertical mean error and Root Mean Square Error (RMSE) of TanDEM-X DEM was less than ± 0.20 m, and 1.4 m, respectively, with an excellent absolute 90% linear height error below 2 m. Another study showed that the absolute height error was ± 1.61 m and the relative height error was 1.05 m for TanDEM-X [48].

3.1.2. ASTER GDEM V2

The ASTER is a Japanese sensor onboard on NASA's Terra platform launched into earth orbit in 1999. The instrument provides high-resolution images of the earth in stereo-pairs with the nadir and off-nadir look angles. These stereo-pairs produce digital elevation models globally [49,50]. The improved GDEM V2 adds 260,000 additional stereo-pairs, which improves coverage and reduces the occurrence of artifacts (<https://ssl.jspacesystems.or.jp/ersdac/GDEM/E/>). The refined production algorithm provides improved spatial resolution, increased horizontal and vertical accuracy, and increased superior water body coverage and detection [51]. The ASTER GDEM V2 maintains the GeoTIFF format and the same gridding and tile structure as V1, with 30-meter postings and 1×1 -degree tiles. Santillan et al., 2016 [51], reported that RMSE for vertical accuracy of ASTER GDEM2 was ± 13.25 m.

3.1.3. AW3D30

The panchromatic remote sensing instrument for stereo mapping (PRISM), which is one of the Advanced Land Observation Satellite (ALOS) onboard sensors, was designed to collect worldwide high-resolution stereoscopic topographic data. The uniqueness of the ALOS-equipped Greedy Perimeter Stateless Routing (GPSR) and Satellite Transportable Terminal (STT) instruments includes the ability of automatic determination of the exterior orientation parameters of PRISM geometry without ground control points (GCPs) [52]. PRISM line sensors consist of multiple Charge Coupled Device (CCD) units (6 units for Nadir, 8 units for both forward direction sensor and backward direction sensor) and each CCD unit has approximately 5,000 detectors with a maximum of four consecutive CCD units. Each of the four sensors is used for the triplet stereo observations [51]. Takaku and Tadono [53] revealed that the absolute accuracy of AW3D30 data was about 1.9~2.3 m RMSE for horizontal accuracy and 2.1~3.4 m RMSE for vertical accuracy (https://www.eorc.jaxa.jp/ALOS/en/aw3d/index_e.htm).

3.1.4. Landsat-8 OLI/TIRS

Landsat-8 Operational Land Imager (OLI) data were acquired on 14 April 2013 for LULC classification and from November 2013 to May 2014 for LST retrieval, respectively (<https://earthexplorer.usgs.gov/>). Landsat images are constantly improving by the richness in spectral, spatial, radiometric, and temporal resolution [54] with the new generations of satellites with improved sensors. The Operational Land Imager (OLI) and Thermal Infrared Sensor (TIRS) are instruments onboard the Landsat-8 satellite, which was launched in February 2013. The satellite collects images of the Earth with a 16-day repeat cycle, referenced to the Worldwide Reference System-2 [55]. Landsat-8 OLI and Thermal Infra-Red Sensor (TIRS) images consist of nine and two spectral bands, respectively. Thermal infrared (TIR) remote sensing provides a unique method for obtaining LST information at the regional and global scales since most of the energy detected by the sensor in this spectral region is directly emitted by the land surface [56,57]. According to Wessel. B et al. [47], the error level is about 4%-5% in the thermal band number 10. The error level is about 8%-9% in thermal band number 11 of Landsat-8. In this study, mean LST was calculated for seven months using summer and winter season images from November 2013 to May 2014.

3.1.5. Reference Data

Ground-based building height information was collected from Capital City Development Authority (RAJUK). The building height data were collected by the ground survey by RAJUK until December 2018. The ground-based building height information was obtained from Ground Control Points (GCPs) and digitization of area of individual buildings [58,59]. A high spatial resolution DSM and Digital Terrain Model (DTM) were generated for DMA using ground-based height information. The DSM was verified by ground-based height data and Google Earth images. Some errors were observed in the DSM database such as the DSM values of surrounding single high-rise structures that were shown to be relatively higher than the actual data. All DSMs were co-registered with the referenced ground-based DSM using the map registration module in ENVI software. These databases were referenced to the Universal Transverse Mercator (UTM) zone 46N and World Geodetic System (WGS84) horizontal datum. Later, Google Earth images were also used for overcoming the drawbacks of the open-access global DEMs (AW3D30 and ASTER) acquired in different years. About 40 permanent building structures with no change over time were selected for comparing DSM values to overcome the difficulty of rapidly growing cities with temporal changes in building height [60,61].

3.2. Method

Figure 4 illustrates a simplified flowchart of the methodology and processing of various data sources. Building height was estimated using three types of DSM. Therefore, Landsat-8 data were used to estimate built-up area and TIRS band of Landsat-8 was used to estimate LST. A brief description of the methodology is given below.

3.2.1. Vertical Growth Assessment

Vertical growth refers to the vertical development of the city as well as to the construction of high-rise buildings [62]. In this study, building height was estimated using the Digital Building Height (DBH) model to assess the vertical development of DMA. The extracted building height was validated with ground-based building height data as described below.

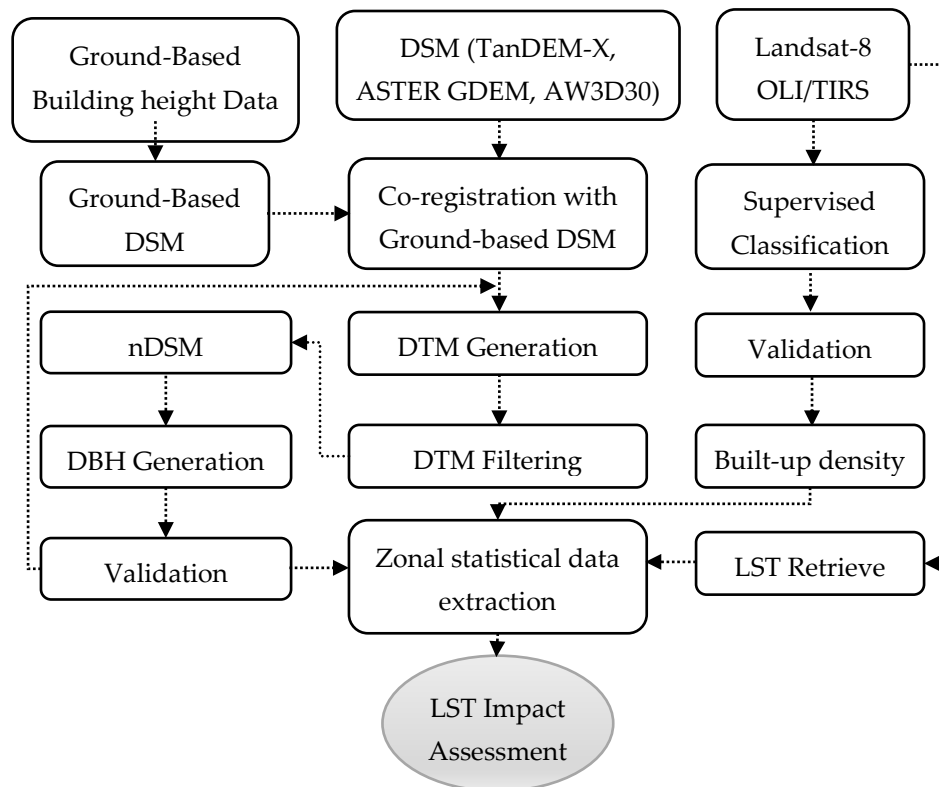


Figure 4. Outline of the methodology adopted.

3.2.2. Building Height Extraction

Building height was extracted by generating DBH, i.e., the normalized DSM (nDSM) over the built-up class pixels. The nDSM was calculated as the difference in elevation values between the Digital Surface Model (DSM) and DTM (digital terrain model, also known as a bare earth model). It is essential to distinguish non-ground pixels and ground pixels by generating DTM. Many approaches are used to generate Digital Elevation Model (DEM) from DSM using a multi-directional processing and slope-dependent filtering technique called “MSD filters”. Although these approaches are effective for high accuracy DTM extraction. However, they are generated by the coarse DSM resolution [63–65]. In this study, the morphological approach MSD filtering technique was used for DTM generation. By using four parameters, which include the Gaussian smoothing kernel size (100 m), the scan line filter extent (100 m), the height threshold (3 m), and the slope threshold (300), the ground and non-ground pixels were distinguished. In addition, a linear interpolation technique was used for all DSM to fill the gaps in generating DTM values. Thereafter, DSM was subtracted from DTM for nDSM generation. Subsequently, vertical accuracy was also assessed by conventional statistical metrics. Many previous studies have used advanced approaches for validation. However, due to the coarse spatial resolution DSM, the pixel-based and object-based height accuracy assessment approaches were used by statistical metrics in this study. The mean height was considered for the footprint of each building. Figure 5 illustrates the building height data based on ground information (Figure 5a), TDX-DSM extracted DBH (Figure 5b), ASTER-GDEM extracted DBH (Figure 5c), and AW3D30 extracted DBH (Figure 5d). According to ground data, the selected building height is about 26 m while TanDEM-X, ASTER-GDEM, and AW3D30 data were estimated at 24.5 m, 18 m, and 19.12 m, respectively.

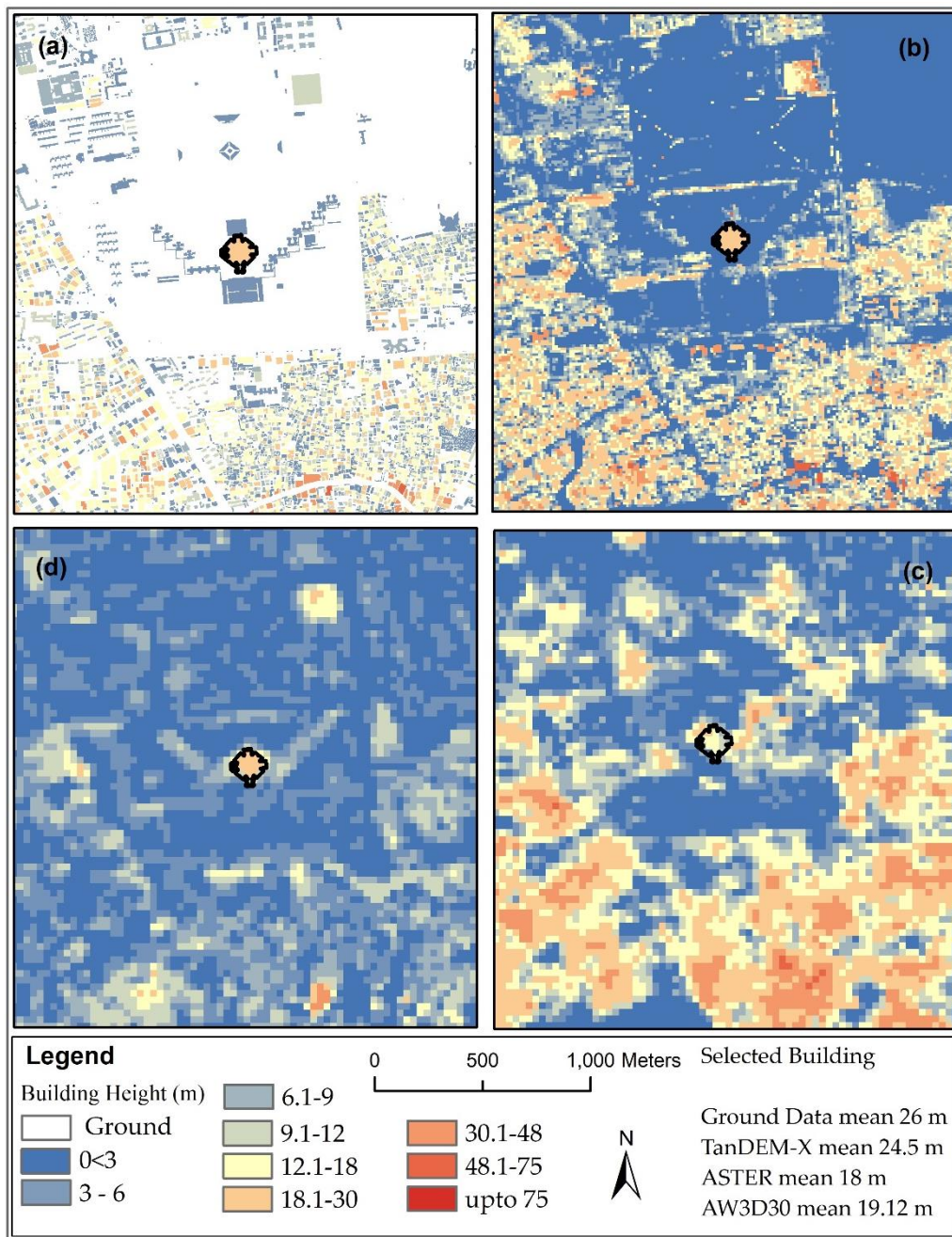


Figure 5. (a) Ground/referenced height, (b) TanDEM-X height Data, (c) ASTER height, and (d) AW3D30.

3.2.3. Built-Up Density (BUD) Analysis

The built-up density is an important indicator for measuring the horizontal spatial growth of the city. The urban built-up area indicates the areas within a city that are already built-up, under construction, and mostly impervious surfaces [66]. A simple equation was used to calculate the built-up density.

$$BUD = \text{built up area of } x / (\text{total area of } x) \tag{1}$$

where x is the small unit (ward number) of the study area.

The built-up area was extracted from Landsat-8 OLI images using the Support Vector Machine (SVM) supervised classification algorithm [67] in ENVI 5.3, as SVM has been shown to provide better results when limited training samples are available [68]. In this research, a single-pixel classification was used under featured engineering using the SVM classifier, which was also applied in the previous

study [69]. Training samples were collected based on the Landsat image supporting with ground-based data. Thereafter, following the Zhang and Tang study [69], the first eight bands (Band 1 to 8) of Landsat-8 were employed for image classification. Table 3 describes the typology of different land cover types and their descriptions. A total of 213 training samples were used in the built-up area, water bodies, vegetation, agriculture, and bare land/sandy area for image classification. Figure 6 shows the LULC map of the study area. Most of the area covered with a built-up area was followed by bare land. After the LULC classification, the result was verified using Google Earth Pro. A total of 85 samples were used for the accuracy assessment. The kappa coefficient was 0.838 with overall accuracy (OA) of 85.8%, user accuracy (recall) of 89%, and producer accuracy (precision) of 81%. Zhang and Tang [67] introduced that SVM and Random (RF) classifiers are most efficient for built-up area extraction. In their study, they compared three classifiers including overall accuracy of 0.849, 0.887, and 0.841 for SVM, RF, and a patch-based approach, respectively. Classification accuracy also acknowledged their findings.

Table 3. Land cover topology.

Land Cover Types	Description
Built-up area	All infrastructure, settlement, road
Bare Land	Fallow land, dry soil, sand filling
Non-built-up area	Natural vegetation, parks, agricultural land, wetland, pond, canal, river, marshy land

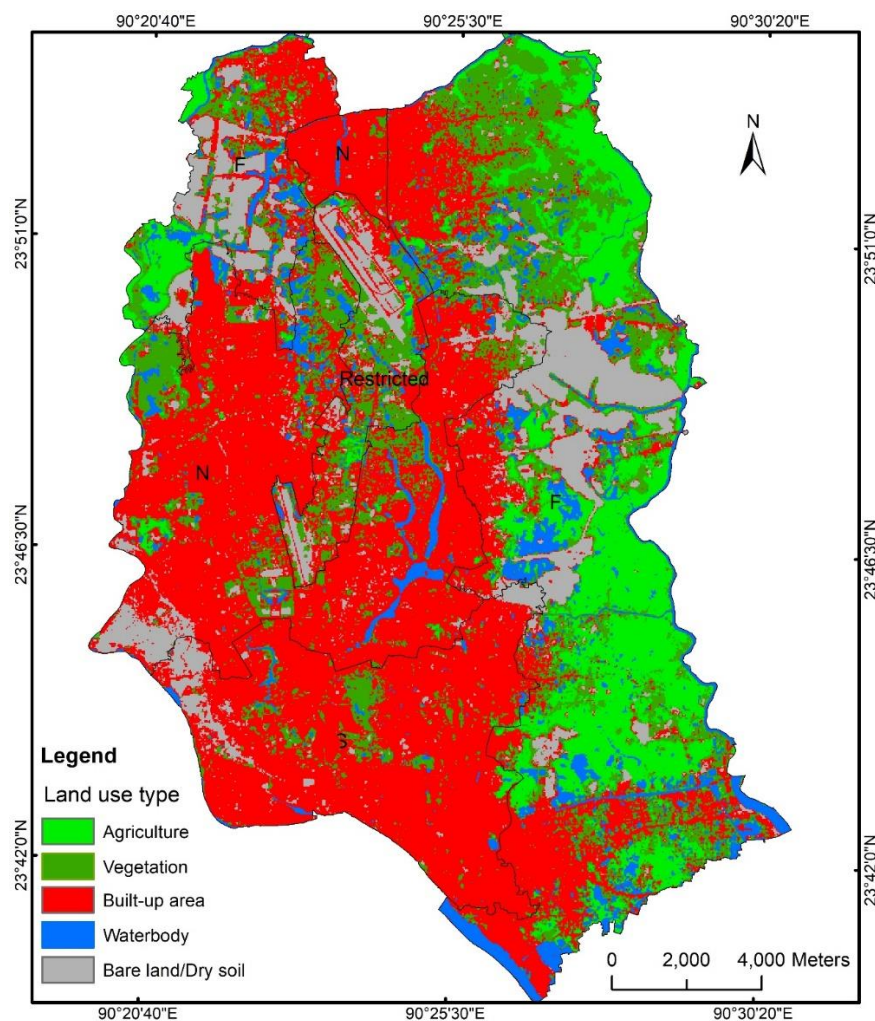


Figure 6. Land use land cover (LULC) map for the year of 2013, in map N, S, and F refer to Dhaka North City Corporation (DNCC), Dhaka South City Corporation (DSCC), and fringe area, respectively.

After estimating building height and built-up density, a landscape pattern map was also generated based on the building height and BUD. Buildings were classified by the height and the density of the area in which it is located. The BUD was classified into three classes called low (<40%), medium (40% to <70%), and high ($\geq 70\%$). Similarly, building heights were also classified into three classes named low (<18 m), medium (18 to <48 m) and high (≥ 48 m). Based on these classifications, a total of nine types of buildings were classified.

3.2.4. Land Surface Temperature (LST) Retrieval

Landsat 8 Thermal Infrared Sensor (TIRS) data, which measure the energy emitted from the earth's surface, were downloaded from the US Geological Survey (USGS) Earth Explorer. Cloud-free Landsat-8 data were downloaded from November 2013 to May 2014 in winter and summer seasons. TIRS has two longwave thermal bands, band 10 and 11 (10.3–11.3 μm and 11.5–12.5 μm , respectively), which can be used to retrieve LSTs. To transform reflected solar energy into LST, the radiometric calibration tools of ENVI 5.3 (IDL) were used. Band 10 of TIRS was used because of less effect by the stray light issue [55].

In this research, a two-step process was used to retrieve LST from the Landsat-8 considering unknown land surface emissivity (LSEs) [70]. The heterogeneous land surface has variations in the emissivity from different surface types. In this research, stepwise LST retrieval methods were followed. In the first step, the brightness temperatures were calculated by employing atmospheric correction and spectral radiance. In the second step, LSEs were calculated ranging from 0-1 of different land covers based on the literature review [36]. The top of atmospheric (TOA) spectral radiance (L_γ) were calculated by using the following equation.

$$\text{Radiance } (L_\gamma) = M_L * \text{Band 10} + A_L \quad (2)$$

where M_L represents the band-specific multiplicative rescaling factor, and A_L represents the band-specific additive rescaling factor. M_L and A_L can be obtained from the header file of the image, $M_L = 0.0003342$, $A_L = 0.1$.

Regarding the effective at-satellite temperature of the viewed Earth-atmosphere system, under the assumption of a uniform emissivity, spectral radiance could be converted to brightness temperature obtained by the following equation [39].

$$T = \frac{K2}{\ln\left(\frac{K1}{L_\gamma} + 1\right)} - 273.15 \quad (3)$$

where T is the effective at-satellite brightness temperature in $^\circ\text{C}$. $K1 = 774.8853$ (watts/($\text{m}^2 \cdot \text{ster} \cdot \mu\text{m}$)) and $K2 = 1321.0789$ (kelvin) are calibration constants (this can be obtained from the header file of the image), and L_γ is the spectral radiance in watts/($\text{m}^2 \cdot \text{ster} \cdot \mu\text{m}$).

The classification-based emissivity method (CBEM) is the simplest method in terms of processing and it can provide accurate LSEs for LST retrieval as long as the land surfaces are accurately classified, and each class has a well-known LSE [71]. A surface emissivity layer was created from reference values for various land covers employed by other studies [36]. By using the following equation, LST can be retrieved based on brightness temperature (T) and surface emissivity [37].

$$LST = \left(\frac{T}{1 + .00115 * \frac{T}{1.4388} * \ln(\varepsilon)} \right) \quad (4)$$

where ε is the surface emissivity.

The spatial statistical tool of ArcGIS platform was used for the mean temperature calculation of the study area. November 2013 to May 2014 Landsat-8-based LST were derived to explore the seasonal variations in the study area. Based on the previous study by Shahid, 2010 [41], we considered the

summer season from March to May and the winter season from November to February, respectively. The findings were validated using the ground-based temperature data from the meteorological station.

3.2.5. LST Impact Assessment

LST can be affected by both two-dimensional (2D) and three-dimensional (3D) urban growth. According to literature, many studies have looked at the impact of horizontal morphology. However, few studies have explored the relationship between vertical morphology and temperature, especially at the city scale. In this study, a non-parametric correlation was investigated for assessing the build-up density and building height impacts on LST. Therefore, 3D surface plots were also generated to investigate the relationships among the three variables in the plot.

4. Results

4.1. Building Height

The geo-statistical based comparative analysis of DBH extracted from three DSMs (TanDEM-X, ASTER, and AW3D30) and ground-based building height is presented in the figures (Figure 7, Figure 8, and Figure 9) for the Dhaka South City Corporation (DSCC), Dhaka North City Corporation (DNCC), and fringe area, respectively. The purpose of the comparison is to find out the most suitable DSM for building height extraction. Figure 7 illustrates that the mean building height extracted by ASTER-DSM was greater than TanDEM-X, AW3D30, and also greater than the ground-based building height data. In highly dense areas, where buildings of lower height are shielded by the taller buildings, are difficult to separate by coarse resolution DEM data. The mean building height extracted by ASTER-GDEM reveals an overestimation of 2 to 10 m than the ground-based building height data. The mean building height extracted by TanDEM-X reveals the similarity with ground-based building height data except for the ward numbers S-03, S-09, and S-13 of DSCC. Because of the faster vertical urban development, the TanDEM-X-based DBH shows 3 to 6 m underestimation than the ground-based building height data in the ward numbers S-03, S-09, and S-13. On the other hand, some wards like S-28 to S-35 shows 2 to 3 m overestimation than the ground-based building height data because of the homogeneity effects present in the high-density areas. The homogeneity effect misleads the height variation and this effect increases with the decreasing spatial resolution of the satellite data. Mean building height extracted by AW3D30 spectacles are comparatively less accurate than TanDEM-X and ground data. AW3D30 based DBH shows 3 to 7 m underestimation as compared to TanDEM-X and ground data.

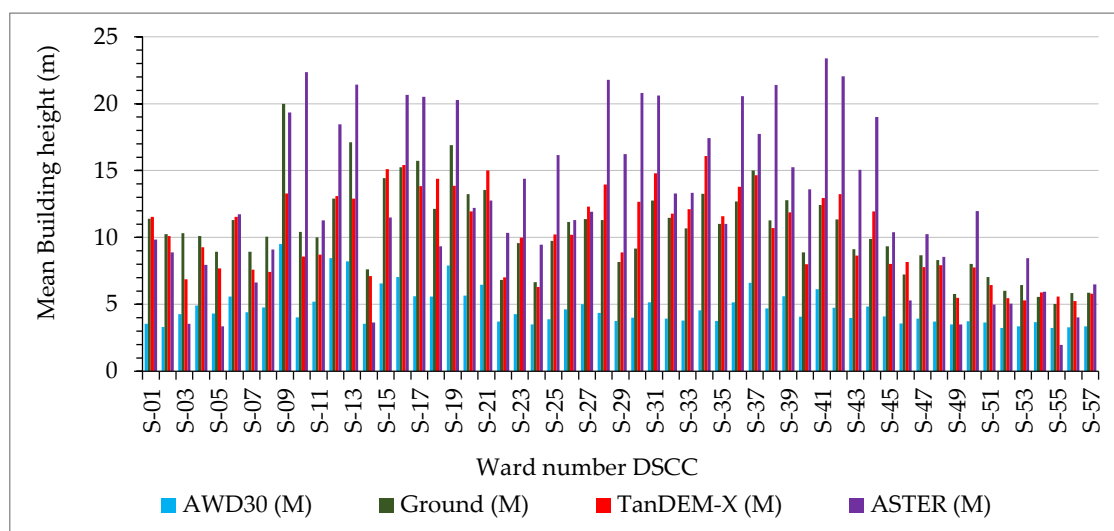


Figure 7. Ward-wise (small administrative boundary) mean building height of Dhaka South City Corporation (DSCC).

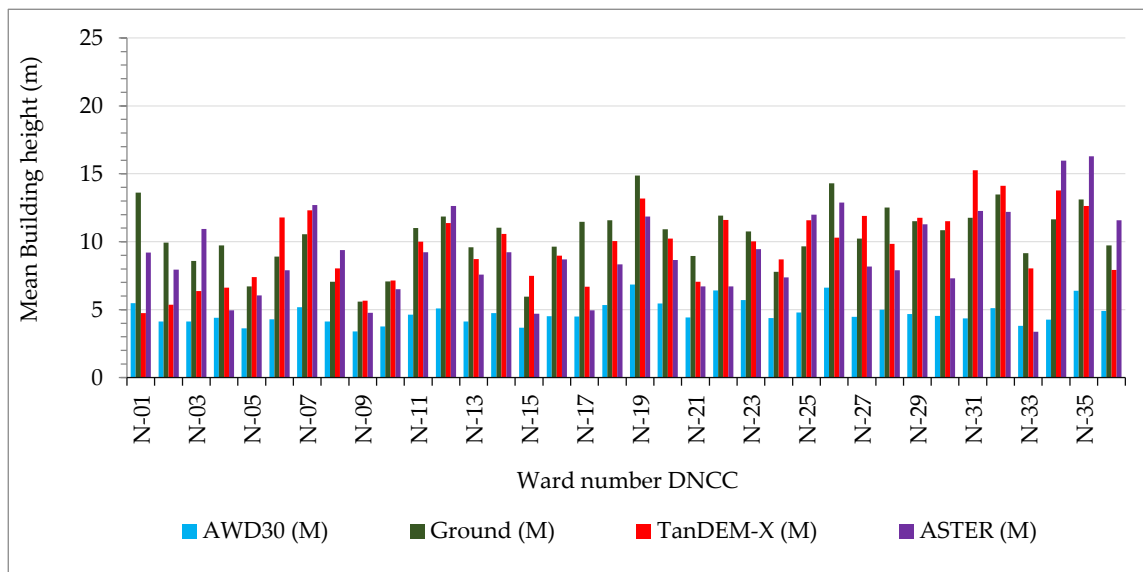


Figure 8. Ward-wise (small administrative boundary) mean building height of Dhaka North City Corporation (DNCC).

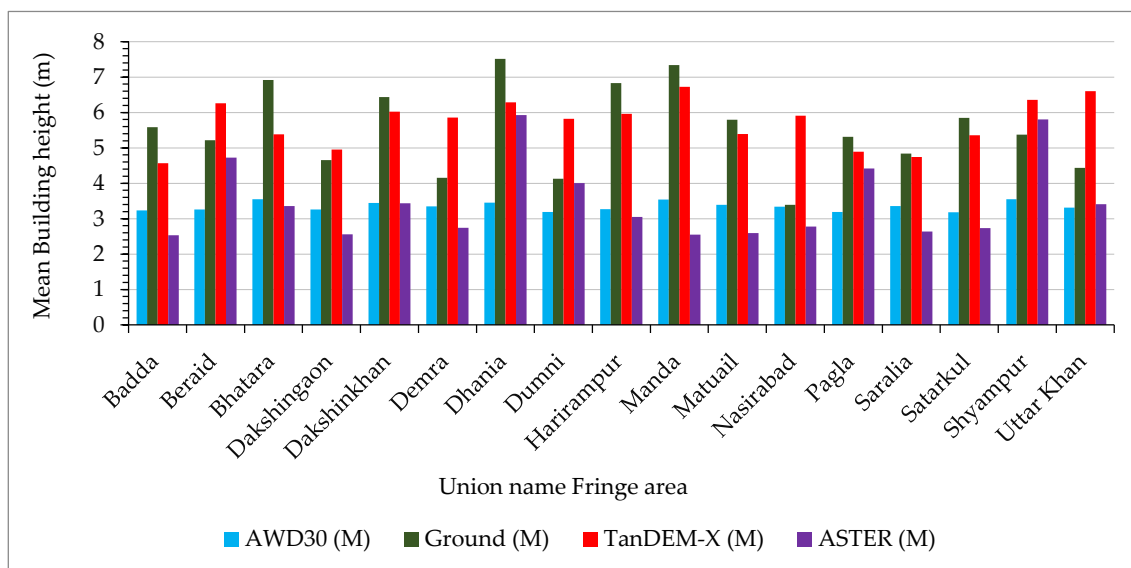


Figure 9. Union-wise (small administrative boundary) mean building height of the fringe area.

Figure 8 illustrates the mean building height extracted by ASTER DSM, AW3D30, and TanDEM-X with respect to ground-based building height data in the DNCC area. The DNCC area is characterized by a less dense building area when compared to the DSCC. The planned areas of Uttara (N-01), Bashundhar (N-17), and Basila (N-33) are growing rapidly, which results in the mean building height being underestimated in comparison to ground data by all datasets. It is understood that building height using AW3D30 was comparatively less accurate in comparison to TanDEM-X and ground data. The estimated building height using AW3D30 shows a 3 m to 8 m difference than ground data where TanDEM-X shows by 1 m to 5 m except ward no. 01 and 02. These two wards are newly developing areas where backdated satellite data are underestimated when compared to ground-based data.

Figure 9 illustrates the mean building height in the Fringe areas is about 2.5 m to 7 m. Surprisingly, the mean height estimate by AW3D30 data was almost linear in the fringe area. This is because the fringe area was covered by limited/no buildings during the acquisition of AW3D30 data. ASTER data showed lower building height value than ground data, which was about 1.5 m, 2 m, 2.5 m, and 2.6 m, respectively, in Dakshingaon, Manda, Matuail, Saralia, and Satarkul unions. Due to the rapid growth pressure in the fringe area, many buildings have been constructed in this area after the acquisition of ASTER data. However, the mean building height extracted by TanDEM-X was compatible with the ground-based building height data except for Nasirabad, Demra, Dumni, and Uttar Khan unions.

Figure 10 illustrates the vertical growth of DMA. Mean building height extracted from TanDEM-X data matches well with ground-based building height data. It also revealed that the distribution of building height in DSCC is marginally higher than DNCC, which was about 10.02 m or about the height of a three-story building. The fringe area is characterized by lower height values, i.e., the value of 4.98 m or approximately smaller than a two-story building. The mean building height is lower in the fringe area and higher in the DSCC area, which was ascertained by all data.

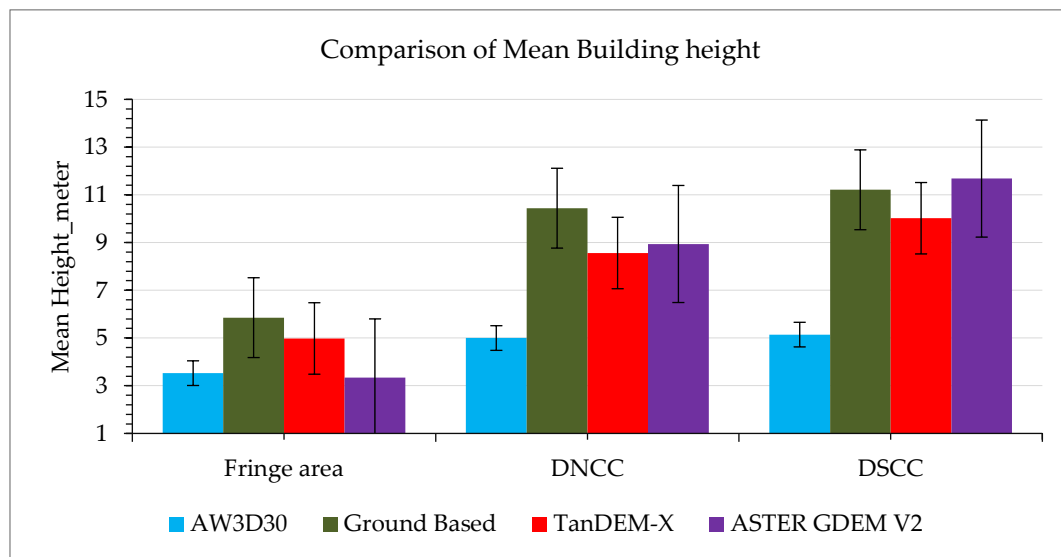


Figure 10. Mean vertical growth of DMA. The Y-axis shows building height by meter and the X-axis shows three zones of the study area.

4.2. Built-Up Density and Landscape Pattern

Figure 11 and Table 4 reveals the percentage of LULC classes (Figure 11a) and built-up density (Figure 11b) for the three zones of the DMA, i.e., DNCC, DSCC, and fringe area. Figure 11 also reveals that, in 2013, the built-up area is covered by 47% of the DMA, which is followed by the bare land of 32%, agriculture of 12%, vegetation of 7%, and waterbody of 7%. The highest percentage of built-up density is in the DSCC area, which is about 94%. The lowest percentage is in the fringe area, which is about 44%. The horizontal growth of Dhaka city is mainly occurring in the fringe area because of the availability of non-built-up areas at the core city. The areas that are more impervious with less landfill/sand fill and a non-built-up area are observed at the core (DSCC and DNCC) city areas, which also suggest that horizontal growth follows a process wherein wetland/vegetation is converted to sand fill and, subsequently, converted to the built-up area. A previous study by Ahmed [39] stated that the average built-up area of the DMA was about 37%, which is followed by the bare land of 45%, water body of 9%, and vegetation of 8% using Landsat-5 data (acquisition year 2009). Since the population pressure is continuously increasing along with industrial development that causes a rapid rate of increase in built-up areas. The DMA area has lost agricultural land, vegetation, and water bodies by 0.5%, 31.1%, and 10%, respectively, from 2002 to 2014 [72].

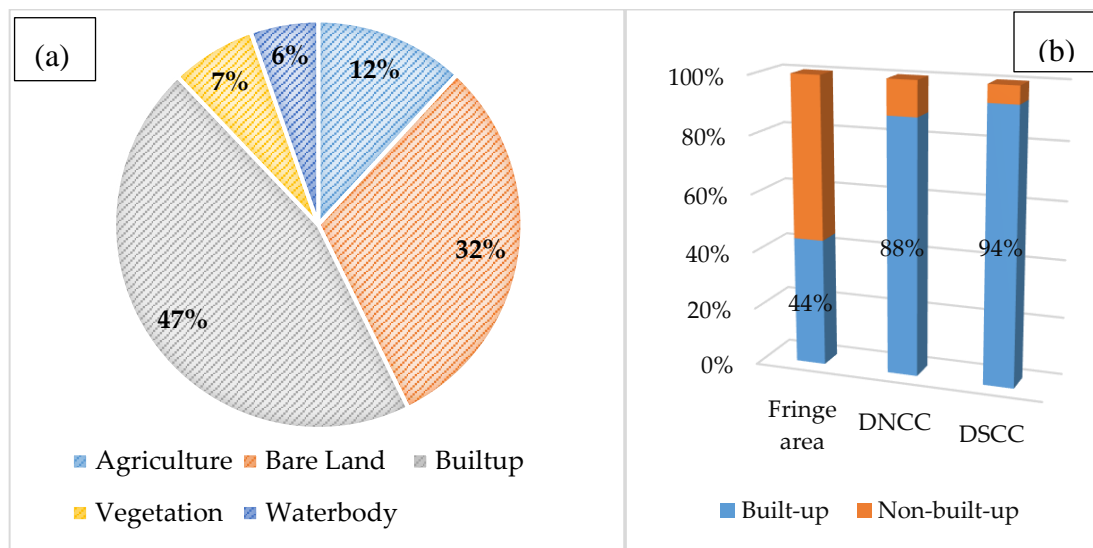


Figure 11. (a) Pie chart with the percentage of different land use land cover (LULC) classes and (b) built-up ratio shared by the Dhaka Metropolitan Area (DMA).

Table 4. Landscape pattern.

	Low Density (<40%)	Medium Density (40% to <70%)	High Density (>70%)
Low height (2.5 m to <19.6 m)	11%	38%	35%
Medium height (19.6 to <52.48m)	1%	7.5%	7%
High height (>52.8m)	0.05%	0.07%	0.12%

Figure 12 illustrates the landscape pattern of the built-up area generated by building density and height. The fringe area was characterized by low density (<40%) and building height was also low (<18 m). Medium (18 to <48 m) and tall (>48 m) buildings were concentrated in the DSCC and DNCC areas where building density was also high. Statistical data of building area classification revealed that about 38% of total building areas are under the ‘Low height (2.5 m to <19.6 m)-Medium density (40% to <70%)’ class, which is followed by 35% for ‘Low height (2.5 m to <19.6 m)-High density (>70%)’, 11% for ‘Low height (2.5 m to <19.6 m)-Low density (<40%)’, 8% for ‘Medium height (19.6 to <52.48 m)-Medium density (40% to <70%)’, and 7.5% for ‘Medium height (19.6 to <52.48 m)-High density (>70%)’. The high height (>52.8 m)-high density (>70%) was only 0.12% of the total building areas.

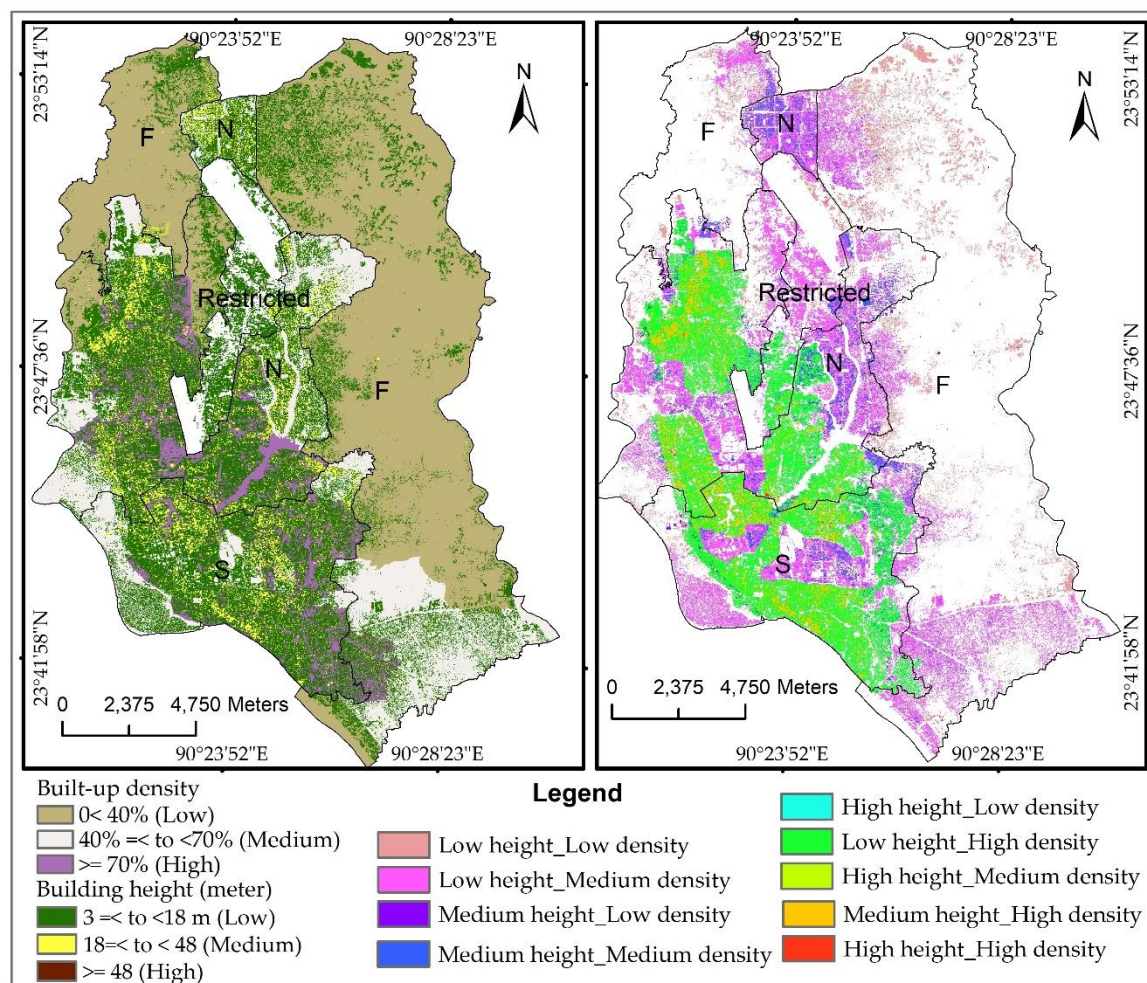


Figure 12. The left side shows the built-up density and building height, while the right side shows the building type based on building height and density. In the map N, S, and F, refer to DNCC, DSCC, and fringe area, respectively.

4.3. Land Surface Temperature (LST)

Figures 13 and 14 illustrate the variations of LST in DSCC, DNCC, and fringe area in comparison with the meteorological data of DMA from November 2013 to May 2014. The findings reveal that the highest LST (36.5 °C) was found in March (summer season). On the other hand, the lowest LST (22.2 °C) was found in December (winter season). The highest maximum (36.5 °C) and the lowest minimum (22.2 °C) LST value was in the fringe area and the lowest maximum (34 °C) and the highest minimum (22.2 °C) LST value was in the DSCC. The statistical data shows a standard deviation of about 1.51 °C, 1.24 °C, and 1.07 °C, respectively, in the fringe area, DNCC, and DSCC during the summer season. On the other hand, the standard deviation was about 1.33 °C, 0.73 °C, and 0.69 °C, respectively, in the fringe area, DNCC, and DSCC during the winter season. However, this difference was highest during the summer season. The maximum temperature difference in the fringe area was about 12.5 °C, which is followed by 9.30 °C in the DNCC area and 8.61 °C in the DSCC area during March. The minimum temperature difference in the fringe area was about 8 °C. This is followed by 7 °C in the DNCC area and 6 °C in the DSCC area during December. Singh et al. [73] observed the maximum temperature difference was in agricultural areas, which was followed by rural areas, and urban built-up areas in Delhi. This supports our findings in Dhaka. While the difference between the maximum and minimum temperature was low in the DSCC area, the mean LST was always high in the DSCC area. This is because the higher impervious surface at the DSCC area has a low albedo effect and absorbs most of

the incoming solar radiance in the daytime. However, they re-radiate the absorbed solar energy during the night in the form of thermal heating. Figure 14 reveals that, in the summer season, about 50% area LST range is between 28 to <30 °C and 30% area LST range is between 26 to <28 °C. On the other hand, in the winter season, about 60% area LST range is between 24 to <26 °C. A previous study showed the LST range is between 27 to <30 °C in 44% of DMA in 2009 [39].

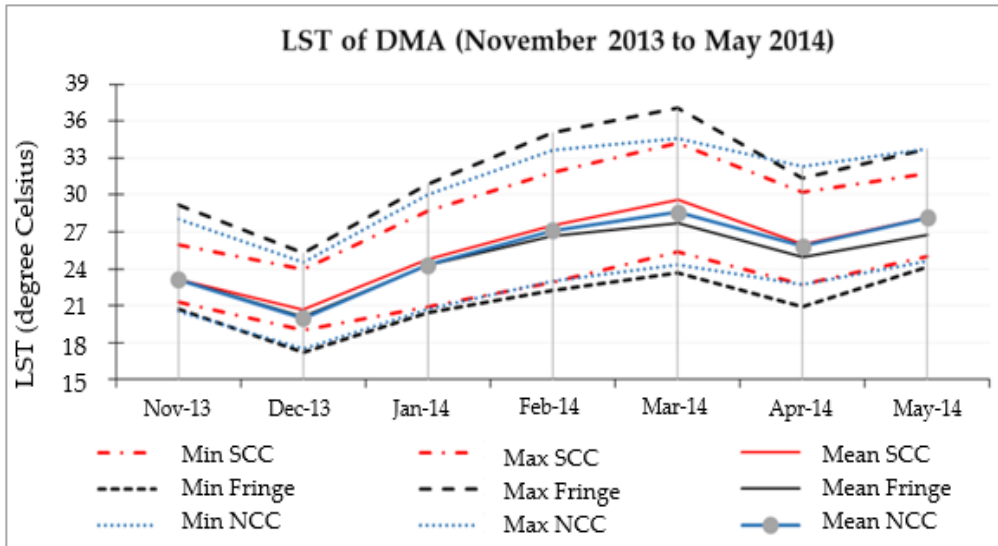


Figure 13. Maximum, Minimum, and Mean LST of DMA with seasonal variation

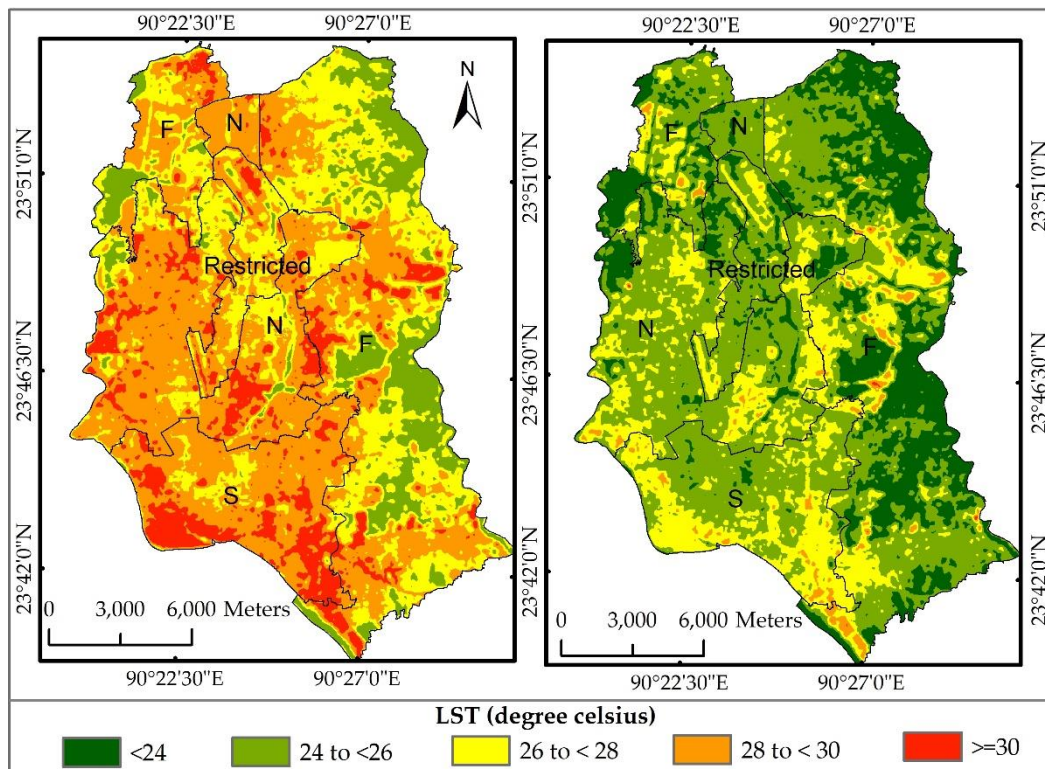


Figure 14. The average of summer (March to May 2014) land surface temperature (LST) (left) and the average of winter (November 2013 to February 2014) LST (right) in the map N, S, and F refer to DNCC, DSCC, and fringe area, respectively.

Figure 15a,b illustrate the average mean LST of DMA in the summertime (March to May) and wintertime (November to February) seasons. It reveals that the median LST was the highest in the DSCC (29.30 °C in the summer and 25.50 °C in the winter) during both seasons, which is followed by the DNCC (29 °C in the summertime and 26 °C in the wintertime) and fringe area (28 °C in the summertime and 25.1 °C in the wintertime). It also reveals that the maximum and minimum LST difference was found in the fringe area. This is followed by the DNCC and DSCC, which can also be understood from Figure 14. However, the maximum and minimum LST differences were higher in the winter season than the summer season of all areas, which was mostly observed in the DSCC and DNCC areas. The statistical analysis revealed the summer and winter season LST differences that are statistically significant (level <0.01).

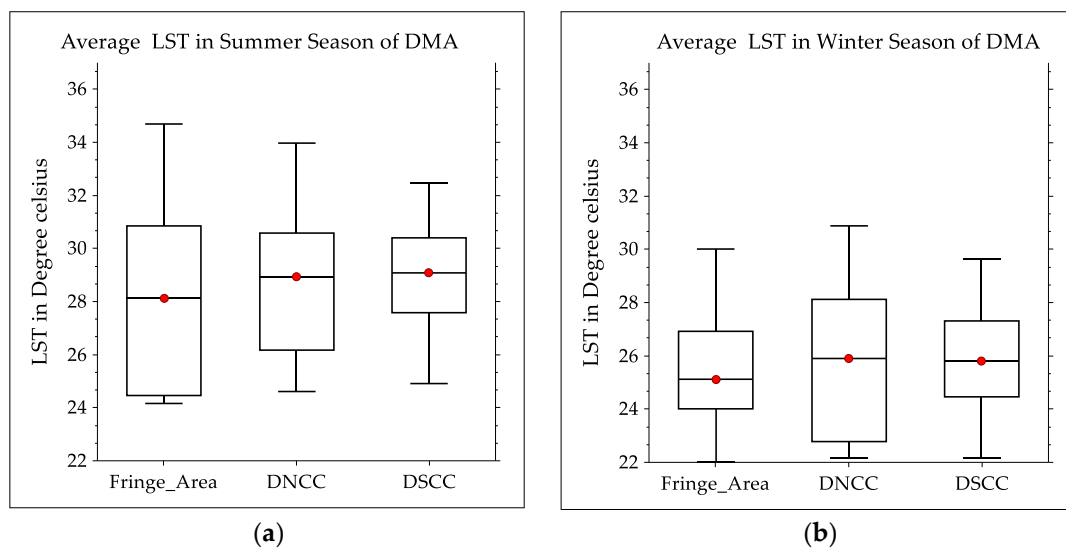


Figure 15. (a) Average LST in the summertime and (b) average LST in the wintertime of DMA.

Meteorological station-based temperature data were used for the validation of the Landsat extracted LST. The meteorological station lies in the “Low Height-High density” area at 23°46′30″N latitude and 90°24′17″E longitude. Monthly mean LST was compared with meteorological station-based ambient air temperature (Figure 16) for the accuracy assessment. The average value by 3 × 3 pixel of Landsat derived LST values were compared with the ground station. Satellite-based LST showed approximately 1 to 6 °C higher than the air temperature (T_{air}) and the differences observed were mostly in November and February. Gallo et al. [74] also observed LST is approximately 1 to 8 °C higher than T_{air} in a cloud-free sky. Because of the cooling effect of urban vegetation, shading and consuming latent heat via evapotranspiration, the presence of vegetation alone can reduce the T_{air} by 1 to 5 °C during the summer season [36]. In the winter season, evapotranspiration happens more slowly than during the summer season, which results in the temperature differences being higher during the winter season.

4.4. LST Impact Assessment

The impact of urban spatial growth on LST was revealed through statistical analysis. Figures 17 and 18 illustrate the impact of built-up density and building height on LST, respectively. The impact of the landscape pattern based on building height and density on LST is represented by the 3D surface plot in Figure 19 and Table 5.

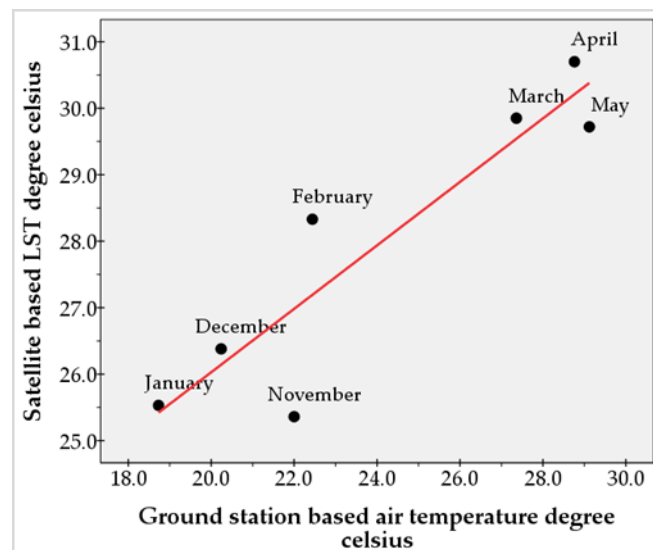


Figure 16. Ambient air temperature (T_{air}) based on a meteorological station and LST measured from Landsat Operational Land Imager (OLI) Thermal Infrared Sensor (TIRS) band 10.

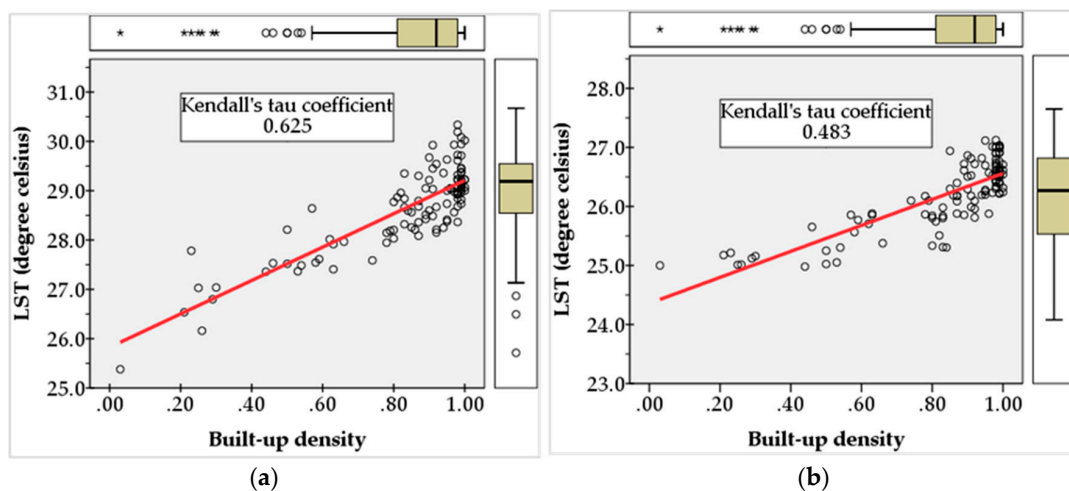


Figure 17. Relationship between (a) built-up density and summer land surface temperature (LST), (b) built-up density, and winter LST where the Y-axis shows LST in degree Celsius, the X-axis shows built-up density, and the red line is the slope of the correlation coefficient.

4.4.1. Correlation Analysis

Figure 17 illustrates the correlation between built-up density and LST. The correlation was higher in the summer season as compared to the winter season. The non-parametric correlation analysis showed the value of Kendall's tau correlation coefficient of LST-built-up density was 0.625 and 0.483 (with significance level <0.01) in the summer and winter seasons, respectively. In the summer, the LST value was mostly concentrated around the trend line, which means a strong correlation. However, some high LST values were found in the less built-up density areas because of the presence of highly responsive thermal surfaces in the fringe area like dry soil/sand filling area and metallic/steel roof. Additionally, low LST values were observed in the highly-dense areas due to the presence of surrounding thermal cooling surfaces of non-built-up areas such as water bodies, green spaces, shadows, and older roofs. Bhargava et al. [5] investigated that the roof and pavement surfaces were hotter than the ambient air during the sunny summer day, while shaded or moist surfaces in rural surroundings remained close to air temperature. In the winter season, the LST values were distributed in a scattered manner along the trend line. It was also observed that, in the low-density areas, LST values were high. However, the LST

value was mostly below the trend line in the dense areas. The downwelling sun’s radiance can directly reach the surface of the low-density areas, which results in an increase in LST in open land, soil, road, bare land, and low-density areas where built-up density is low.

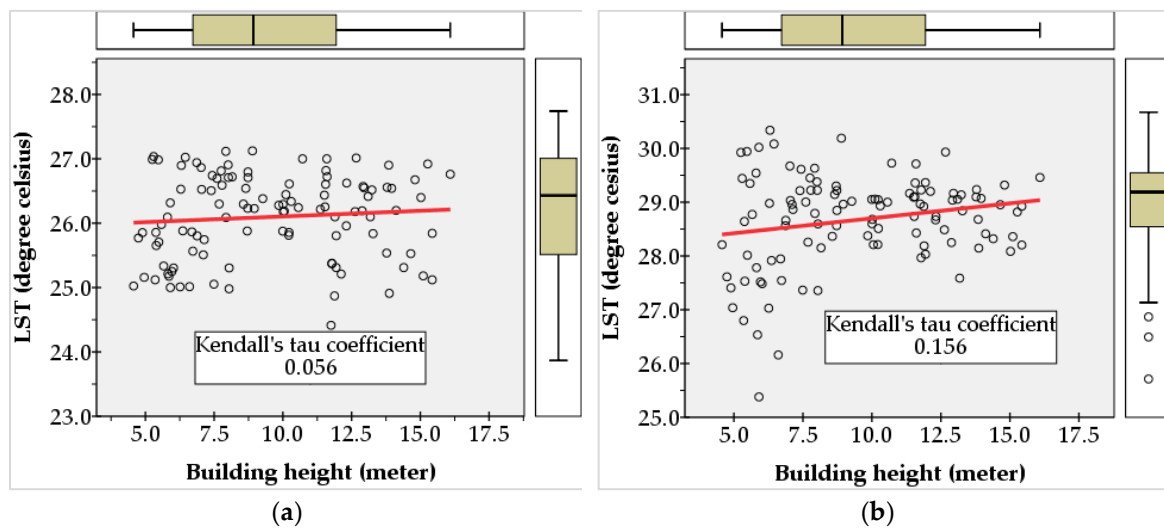


Figure 18. Relationship between (a) building height and summer LST, (b) building height and winter LST where the Y-axis shows LST in degree Celsius, X-axis shows building height, and the red line is the slope of the correlation coefficient.

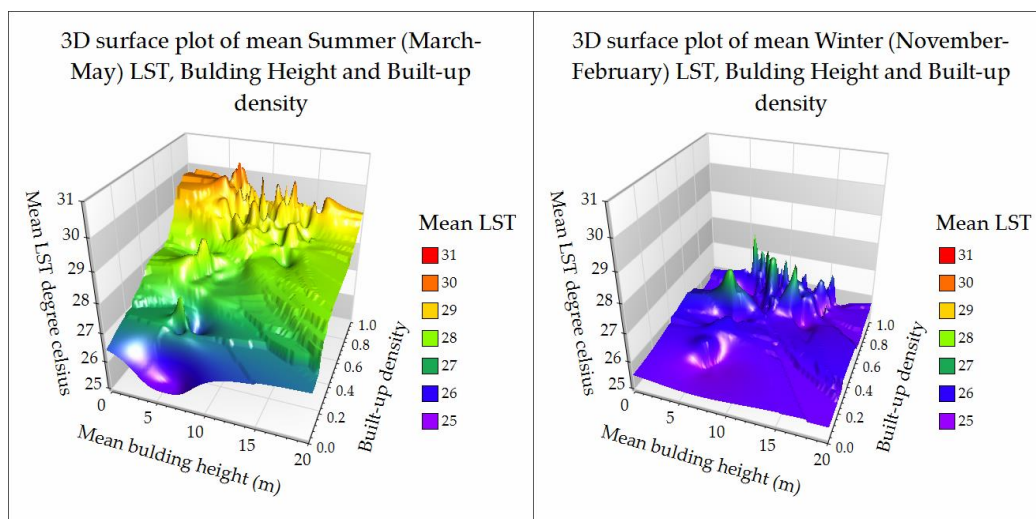


Figure 19. 3D surface plot of LST, building height, and built-up density.

Table 5. LST characteristics of different landscape patterns of the built-up area.

Building Height/Built-Up Density/Mean LST		Built-Up Density					
		High Summer LST		Low	High Winter LST		
Building Height	High	29.32 °C	29.28 °C	29.15 °C	28.03 °C	27.67 °C	27.38 °C
	Medium	29.96 °C	29.42 °C	29.12 °C	28.08 °C	27.57 °C	27.61 °C
	Low	30.24 °C	29.33 °C	28.41 °C	28.32 °C	27.85 °C	26.77 °C

Figure 18a,b illustrate the variation of building height and LST of DMA in summer and winter seasons. It shows that building height has a very weak correlation with LST. However, the LST values shown were more positively correlated with building height in the summer season as compared to

the winter season. The non-parametric correlation analysis showed that the summer LST-Vertical growth and winter LST-Vertical growth Kendall's tau correlation coefficient was, respectively, 0.156 and 0.056 (with the significance level $<.01$). To support the findings of this study, Guo et al. [75] also observed the LST and building height R^2 value was 0.126 in the summer and approximately 0.077 in the winter in Guangzhou city, China. The cause behind this is as follows. In the summer, geometric surface heterogeneous effects respond better than in the winter. In the winter, results revealed a very weak relationship and the LST values were distributed within 22.3 °C to 29 °C without considering building height. However, a significant number of high LST points concentrated in low-height building areas were also observed during both the summer and the winter. Because of metallic roofs in newly developed low-height tin shade houses, new concrete roofs exist in the ward numbers S-24, S-49, S-55, S-56, and S-57. In addition, due to the existence of low-height industrial buildings in Ward numbers S-14, S-52, S-53, N-24, and Shyampur Union, high LST values were also observed in these areas.

4.4.2. Three-Dimensional (3D) Surface Plot

Figure 19 illustrates the three-dimensional surface plot of mean LST, vertical growth, and built-up density of DMA. High LST values were found in high-rise and low-rise buildings of high-density areas. Due to the congested concrete building, metallic rooftops, absent of open spaces in lower height building areas, LST were found to be higher in both seasons. The congested buildings and narrow street canyons prevent solar radiation from heating the streets directly in the daytime [76,77]. Therefore, cooling factors do not work properly in dense urban areas because remote sensing based LST data was directly extracted from rooftop surfaces by disregarding heterogeneous surfaces. On the other hand, low LST values were found in less dense areas for both high-rise and low-rise buildings. In low-density areas, the presence of water bodies, green spaces, streets, and open soil result in a cooler surrounding environment for areas with tall buildings especially in the DNCC area. The lowest mean LST was found in the built-up area (40%) where the mean height was about 3 m in both summer and winter seasons. On the other hand, the highest LST was found in the areas where the building height and built-up ratio were also high. It was also revealed that the LST was high in areas where the building height was low, but the built-up ratio was high (90%).

The highest mean LST was found in the 'Low height-high density' area, which was approximately 30 °C (Table 5). On the other hand, the lowest LST was found in the 'Low height-low density' area in both the summer and the winter. This also acknowledges the results discussed in Section 4.4.2 of this study. The LST value showed gradients from low-density to high-density areas. Similarly, the previous study by Zheng et al. [78] revealed that residential neighborhoods in Beijing city, China have low LST effects compared to low-height buildings. Their study also found that low-height buildings have higher LST than tall buildings. These findings were also confirmed by this study.

5. Discussion

Urban growth (both vertical and horizontal) and its impact on LST was investigated using remote sensing data of DMA. The effect of spatial growth on LST with season variations was also investigated in this study. Four key issues of this study, including the accuracy of building height estimation, built-up density calculation, LST estimation, and LST impact assessment on building height and built-up density are discussed in this section.

Building heights were extracted by employing the Normalized Digital Surface Model (nDSM) and verified by the ground-based building height dataset. With the support of ground-based data and updated high-resolution DSM, it is possible to obtain more precise building heights as well as vertical growth information. TanDEM-X 12m DSM data offered better accuracy than other low-resolution DSMs such as AW3D30 and ASTER (GDEM). Dense building areas offer the maximum frequency of height error where a low height building is covered by the tall building, which results from the inclination effect of the satellite image [79]. Since the average building height of DMA is about 9 m, the AW3D30 offers the maximum height error (3 to 7m). It is suitable for estimating building

height taller than 9 m [80]. High-resolution DSM is more efficient in estimating building height than low-resolution DSMs. However, DBH generation is still a challenge using outdated and low-resolution DSM, especially in rapidly growing cities. This is because, in the fringe or peripheral area of rapidly growing cities, the spatial growth rate is very high, which makes it difficult to estimate building height using previous years' data. Apart from that, due to the increase of multiple scattering effects and small dimensions of buildings, it is problematic to extract building height using low-resolution DSMs in the densely built-up urban areas. Furthermore, due to the differences in ground elevation, the irregular elevation of rooftops, building shadow effect, inaccurate DSM filtering, assumption of flat ground and rooftops, the congested neighbor building effect cannot delineate the individual structure efficiently. Therefore, building heights are sometimes overvalued or underrated. To overcome these challenges, a morphological approach MSD filtering technique was used for DTM extraction. Moreover, the DSM was masked by road network data because this urban feature mostly lies on the ground surface and can be used as additional terrain reinforcement information. Low or medium resolution data can provide a valuable source of building height information in studying vertical expansion on a large scale if high-resolution data are not available.

By employing Landsat 8 data, the built-up area was extracted using SVM classifier to estimate built-up density. All infrastructure and settlements were classified as built-up areas. It is difficult to further classify these built-up areas into residential, commercial, and industrial areas using 30 m resolution data. However, to reduce this limitation, the landscape pattern of the built-up area based on building height and built-up density is expedient for realizing the development pattern of DMA. Previous studies investigated the relationship between LST and Local Climate Zone (LCZ) using the World Urban Database and Access Portal Tools (WUDAPT) scheme [81,82]. In their study, they used a training sample for LCZ mapping assisting with Google Earth Engine, Google Street view, and NDVI (Normalized Difference Vegetation Index) data. Therefore, a total of 17 types of LCZ were classified using random forest classifiers based on the hypothesized training sample. Their study did not focus to quantify the building height scientifically and landscape pattern accordingly. Apart from that, the coverage of Google street view data is not available for global cities and also not well attributed. However, the proposed method in this study is more holistic and informative for urban planners in city-shaping.

LST was retrieved from November 2013 to May 2014 to explore the seasonal variation of LST. The mean LST was low in the fringe area than DNCC and DSCC because of the existing dry soil, sand, and impervious areas that reflect more solar radiation. Apart from that, natural features in the fringe area can retain thermal energy by evapotranspiration, which can reduce the amount of thermal energy that reaches the surface and gets emitted into the atmosphere [24]. On the other hand, the spectral response of thermal energy in the core city area is high because of the presence of more impervious areas [83]. The highest mean LST was at the DSCC area because of having more impervious areas, congested buildings, albedo effects, and low air circulation [84]. The LST is highly affected by seasonal variations in both the core city area and its surroundings because of low down-welling radiance in the winter (November to February) and high down-welling radiance in the summer at the mid-latitude tropical region [85].

Building density has a strong positive correlation to LST than building height, and this correlation is significantly affected by seasonal variations. It was also acknowledged by the previous study in Guangzhou, China [75]. In their study, they concluded that building density has a stronger correlation with LST than building height. They also observed that urban morphology is not only the cause of LST but also has some other factors such as anthropogenic heat, wind speed, rainfall, nearby river or ocean, air temperature, and topography. High building density increases population density, which also increases anthropogenic heat-producing activities. However, this study did not consider the topography, rainfall, and wind speed issues during the LST impact assessment. Han G. and Xu J [38] investigated that high-temperature anomalies were closely associated with built-up land, densely populated zones, and heavily industrialized districts. Moreover, high-rise buildings, glasshouses, congested buildings,

less/no setback areas in the DSCC area, and part of DNCC area are also responsible for high LST in DMA. This study is on city-scale, which is mainly characterized by mixed-use (residential, commercial, industrial), minimal vegetation, dense building area, narrow road width, low land-building ratio, and building materials, which are highly sensitive to solar radiance. This has significant effects on the urban heat island (UHI) effect. The impact of the landscape pattern on LST was also affected by seasonal variations. In both summer and winter seasons, it was noticed that 'low height-high density' building area was responsible for higher LST. On the other hand, the 'low height-low density' building area was responsible for lower LST. Therefore, it is clear that density is the key driver of increasing LST.

The findings presented in this paper suggest that vertical development is better than horizontal development, which provides enough open spaces, green spaces, and preserves natural features. A study by Zheng et al. [78] revealed that higher residential buildings have low LST effects in a neighborhood-scale residential area mixed with residential buildings and enough vegetation, which results in a significant cool island effect. In this context, urban sprawl must be controlled to improve the microclimate environment of DMA. It is also suggested that low-height building areas such as S-43, S-55, S-56, and S-57 desperately demand LST cooling surfaces. Violation of the Floor Area Ratio (FAR) regulation, the absence of height zoning, the absence of Bangladesh National Building Code (BNBC), weak monitoring of development, less attention paid by city planning authorities toward building construction, and unplanned and haphazard spatial growth of the city may be the driving forces of LST in DMA. However, without the appropriate planning tools such as decentralization, green belts, increase in open/green spaces in the core city by redevelopment/land readjustment technique, public awareness about city planning rules/regulations, and increased responsibility of the concerned authorities, it is difficult to stop the adverse impacts of spatial growth. On the other hand, for areas that are already densely built-up, building renovations incorporating green building materials and rooftop greenery can help reduce the LST.

6. Conclusions

In conclusion, this study was the first attempt at observing the effect of spatial city growth (both vertical and horizontal) on LST using satellite remote sensing data and geospatial techniques in the DMA area. The following conclusions, while considering all previous literature, were reached: (a) TanDEM-X DSM offers higher vertical accuracy than other similar satellite-derived DBH, (b) dense built-up areas are highly vulnerable to solar radiation, (c) built-up density vs. LST has a stronger relationship than Vertical growth vs. LST, and (d) LST is significantly affected by seasonal variations. The analyses in this study were conducted using remote sensing data from 2013 to 2014. Further research should pursue more findings to validate this research using more accurate and up-to-date datasets. During the height calculation, the rooftops of buildings were considered flat. In addition, the LST was retrieved without considering day-time and night-time temperatures, humidity, and other factors relating to LST. In addition, the impact of landscape patterns of the non-built up area and urban functional zones on LST was not investigated. Lastly, in future research, it is important to examine more cities while also overcoming the above-mentioned limitations.

Author Contributions: Conceptualization, M.M.R., R.A., P.M., and W.T. Methodology, M.M.R., R.A., A.P.Y., and J.D. Validation, M.M.R. and R.A. Formal analysis, M.M.R. and R.A. Investigation, M.M.R. Resources, R.A. Data curation, M.M.R., R.A. Writing—original draft preparation, M.M.R. and R.A. Writing—review and editing, M.M.R., R.A., A.P.Y., J.D., P.M., W.T., P.K., N.S., B.A.J., R.D., A.K., S.C., and T.A.K. Visualization, M.M.R. and R.A. Supervision, R.A. All authors have read and agreed to the published version of the manuscript.

Funding: This research received no external funding.

Acknowledgments: The authors would like to thank Hokkaido University and Japan Student Services Organization (JASSO) for providing fellowship. We are also thankful to the Global Challenge Research Funds (GCRF) of the University of Glasgow. We are thankful to the German Aerospace Center (DLR) for TanDEM-X data grant DEM_URBAN2809, Japan Aerospace Exploration Agency (JAXA) EORC data grant ER2A2N133, Earth Remote Sensing Data Analysis Center (ERSDAC), and the United States Geological Survey (USGS) for providing satellite data. Authors acknowledge the support of the Capital City Development Authority (RAJUK),

Dhaka, Bangladesh for providing necessary data and information. We appreciate the contribution made by the anonymous reviewers.

Conflicts of Interest: The authors declare no conflict of interest.

References

1. Bek, M.; Azmy, N.; Elkafrawy, S. The effect of unplanned growth of urban areas on heat island phenomena. *Ain Shams Eng. J.* **2018**, *9*, 3169–3177. [[CrossRef](#)]
2. Wong, N.H.; Yu, C. Study of green areas and urban heat island in a tropical city. *Habitat Int.* **2005**, *29*, 547–558. [[CrossRef](#)]
3. Coutts, A.; White, E.C.; Tapper, N.; Beringer, J.; Livesley, S. Temperature and human thermal comfort effects of street trees across three contrasting street canyon environments. *Theor. Appl. Clim.* **2015**, *124*, 55–68. [[CrossRef](#)]
4. Santamouris, M. *Energy and Climate in the Urban Built Environment*; Informa UK Limited: Colchester, UK, 2013.
5. A, B.; S, L. Urban heat island effect: it's relevance in urban planning. *J. Biodivers. Endanger. Species* **2017**, *5*, 5–187. [[CrossRef](#)]
6. Guo, Z.; Wang, S.; Cheng, M.; Shu, Y. Assess the effect of different degrees of urbanization on land surface temperature using remote sensing images. *Procedia Environ. Sci.* **2012**, *13*, 935–942. [[CrossRef](#)]
7. Cuberes, D. Sequential city growth: Empirical evidence. *J. Urban Econ.* **2011**, *69*, 229–239. [[CrossRef](#)]
8. Naserikia, M.; Shamsabadi, E.A.; Rafieian, M.; Filho, W.L. The urban heat island in an urban context: a case study of Mashhad, Iran. *Int. J. Environ. Res. Public Heal.* **2019**, *16*, 313. [[CrossRef](#)]
9. Bonafoni, S.; Keeratikasikorn, C. Land surface temperature and urban density: Multiyear modeling and relationship analysis using MODIS and Landsat data. *Remote Sens.* **2018**, *10*, 1471. [[CrossRef](#)]
10. Mushore, T.D. Linking thermal variability and change to urban growth in harare metropolitan city using remotely sensed data. PhD Thesis, University of Zimbabwe, Harare, Zimbabwe, 15 December 2017.
11. Jalan, S.; Sharma, K. Spatio-temporal assessment of land use/land cover dynamics and urban heat island of Jaipur city using satellite data. *Int. Arch. Photogramm. Remote Sens. Spat. Inf. Sci.* **2014**, *40*, 767. [[CrossRef](#)]
12. Avdan, U.; Jovanovska, G. Algorithm for automated mapping of land surface temperature using LANDSAT 8 satellite data. *J. Sensors* **2016**, *2016*, 1–8. [[CrossRef](#)]
13. Avtar, R.; Tripathi, S.; Aggarwal, A.K.; Kumar, P. Population–Urbanization–Energy Nexus: A Review. *Resour.* **2019**, *8*, 136. [[CrossRef](#)]
14. Hung, W.-C.; Chen, Y.-C.; Cheng, K.-S. Comparing landcover patterns in Tokyo, Kyoto, and Taipei using ALOS multispectral images. *Landsc. Urban Plan.* **2010**, *97*, 132–145. [[CrossRef](#)]
15. Avtar, R.; Aggarwal, R.; Kharrazi, A.; Kumar, P.; Kurniawan, T.A. Utilizing geospatial information to implement SDGs and monitor their Progress. *Environ. Monit. Assess.* **2020**, *192*, 35. [[CrossRef](#)] [[PubMed](#)]
16. Ferdous Jannatul, R.T. Temporal Dynamics and Relationship of Land Use Land Cover and Land Surface Temperature in Dhaka. In Proceedings of the 4th International Conference on Civil Engineering for Sustainable Development (ICCESD 2018), KUET, Khulna, Bangladesh, 9–11 February 2018.
17. Alobeid, A.; Jacobsen, K.; Heipke, C. Comparison of matching algorithms for DSM generation in urban areas from Ikonos imagery. *Photogramm. Eng. Remote Sens.* **2010**, *76*, 1041–1050. [[CrossRef](#)]
18. Avtar, R.; Sawada, H. Use of DEM data to monitor height changes due to deforestation. *Arab. J. Geosci.* **2012**, *6*, 4859–4871. [[CrossRef](#)]
19. Buyantuyev, A.; Wu, J. Urban heat islands and landscape heterogeneity: linking spatiotemporal variations in surface temperatures to land-cover and socioeconomic patterns. *Landsc. Ecol.* **2009**, *25*, 17–33. [[CrossRef](#)]
20. Arnfield, A.J. Two decades of urban climate research: a review of turbulence, exchanges of energy and water, and the urban heat island. *Int. J. Clim.* **2003**, *23*, 1–26. [[CrossRef](#)]
21. Ramaiah, M.; Avtar, R. Urban green spaces and their need in cities of rapidly urbanizing India: A review. *Urban Sci.* **2020**, *3*, 94. [[CrossRef](#)]
22. Grover, A.; Singh, R. Analysis of urban heat island (UHI) in relation to normalized difference vegetation index (NDVI): A comparative study of Delhi and Mumbai. *Environ.* **2015**, *2*, 125–138. [[CrossRef](#)]
23. Groleau, D.; Mestayer, P.G. Urban Morphology Influence on Urban Albedo: A Revisit with the Solene Model. *Boundary-layer Meteorol.* **2013**, *147*, 301–327. [[CrossRef](#)]

24. Taha, H. Urban climates and heat islands: albedo, evapotranspiration, and anthropogenic heat. *Energy Build.* **1997**, *25*, 99–103. [[CrossRef](#)]
25. Yuan, J.; Emura, K.; Farnham, C. Is urban albedo or urban green covering more effective for urban microclimate improvement?: A simulation for Osaka. *Sustain. Cities Soc.* **2017**, *32*, 78–86. [[CrossRef](#)]
26. Maimaitiyiming, M.; Ghulam, A.; Tiyyip, T.; Pla, F.; Latorre-Carmona, P.; Halik, Ü.; Sawut, M.; Caetano, M. Effects of green space spatial pattern on land surface temperature: Implications for sustainable urban planning and climate change adaptation. *ISPRS J. Photogramm. Remote Sens.* **2014**, *89*, 59–66. [[CrossRef](#)]
27. Dousset, B.; Gourmelon, F. Satellite multi-sensor data analysis of urban surface temperatures and landcover. *ISPRS J. Photogramm. Remote Sens.* **2003**, *58*, 43–54. [[CrossRef](#)]
28. Cao, L.; Li, P.; Zhang, L.; Chen, T. Remote sensing image-based analysis of the relationship between urban heat island and vegetation fraction. *Int. Arch. Photogramm. Remote Sens. Spat. Inf. Sci.* **2008**, *37*.
29. Bowler, D.E.; Buyung-Ali, L.; Knight, T.M.; Pullin, A. Urban greening to cool towns and cities: A systematic review of the empirical evidence. *Landsc. Urban Plan.* **2010**, *97*, 147–155. [[CrossRef](#)]
30. Abraham, S. The relevance of wetland conservation in Kerala. *Int. J. Fauna Biol. Stud.* **2015**, *2*, 1–5.
31. Zhang, W.; Li, W.; Zhang, C.; Ouimet, W.B. Detecting horizontal and vertical urban growth from medium resolution imagery and its relationships with major socioeconomic factors. *Int. J. Remote Sens.* **2017**, *38*, 3704–3734. [[CrossRef](#)]
32. Yang, C.; He, X.; Wang, R.; Yan, F.; Yu, L.; Bu, K.; Yang, J.; Chang, L.; Zhang, S. The effect of urban green spaces on the urban thermal environment and its seasonal variations. *For.* **2017**, *8*, 153. [[CrossRef](#)]
33. Ranagalage, M.; Estoque, R.C.; Murayama, Y. An urban heat island study of the Colombo metropolitan area, Sri Lanka, based on Landsat data (1997–2017). *ISPRS Int. J. Geo-Information* **2017**, *6*, 189. [[CrossRef](#)]
34. Avtar, R.; Kumar, P.; Oono, A.; Saraswat, C.; Dorji, S.; Hlaing, Z. Potential application of remote sensing in monitoring ecosystem services of forests, mangroves and urban areas. *Geocarto Int.* **2017**, *32*, 874–885. [[CrossRef](#)]
35. Gage, E.A.; Cooper, D.J. Relationships between landscape pattern metrics, vertical structure and surface urban Heat Island formation in a Colorado suburb. *Urban Ecosyst.* **2017**, *20*, 1–1238. [[CrossRef](#)]
36. Hofierka, J.; Gallay, M.; Onačillová, K.; Hofierka, J. Urban Climate Physically-based land surface temperature modeling in urban areas using a 3-D city model and multispectral satellite data. *Urban Clim.* **2020**, *31*, 100566. [[CrossRef](#)]
37. Mia, B.; Bhattacharya, R.; Woobaidullah, A.S.M. Correlation and Monitoring of Land Surface Temperature, Urban Heat Island with Land use-land cover of Dhaka City using Satellite imageries. *Int. J. Res. Geogr.* **2017**, *3*, 10–20.
38. Han, G.; Xu, J. Land surface phenology and land surface temperature changes along an urban–rural gradient in Yangtze River Delta, China. *Environ. Manag.* **2013**, *52*, 234–249. [[CrossRef](#)] [[PubMed](#)]
39. Ahmed, B.; Kamruzzaman, M.; Zhu, X.; Rahman, M.; Choi, K. Simulating land cover changes and their impacts on land surface temperature in Dhaka, Bangladesh. *Remote Sens.* **2013**, *5*, 5969–5998. [[CrossRef](#)]
40. Hossain, S. Rapid Urban Growth and Poverty in Dhaka City. *Bangladesh e-journal Sociol.* **2008**, *5*, 1–24.
41. Shahid, S. Recent trends in the climate of Bangladesh. *Clim. Res.* **2010**, *42*, 185–193. [[CrossRef](#)]
42. Hordijk, M.; Baud, I. Resilient Cities: Cities and adaptation to climate change. *Media* **2011**, *1*, 111–121.
43. Raja, D.R. Spatial analysis of land surface temperature in Dhaka metropolitan area. *J Bangladesh Inst. Plann ISSN* **2012**, *2075*, 9363.
44. Kosmann, D.; Wessel, B.; Schwieger, V. Global digital elevation model from TanDEM-X and the calibration/validation with worldwide kinematic GPS-tracks. In Proceedings of the FIG Congress, Sydney, Australia, 11–16 April 2010.
45. Rott, H.; Floricioiu, D.; Wuite, J.; Scheiblauer, S.; Nagler, T.; Kern, M. Mass changes of outlet glaciers along the Nordenskjöld Coast, northern Antarctic Peninsula, based on TanDEM-X satellite measurements. *Geophys. Res. Lett.* **2014**, *41*, 8123–8129. [[CrossRef](#)]
46. Hojo, A.; Takagi, K.; Avtar, R.; Tadono, T.; Nakamura, F. Synthesis of L-Band SAR and Forest Heights Derived from TanDEM-X DEM and 3 Digital Terrain Models for Biomass Mapping. *Remote Sens.* **2020**, *12*, 349. [[CrossRef](#)]
47. Wessel, B.; Huber, M.; Wohlfart, C.; Marschalk, U.; Kosmann, D.; Roth, A. Accuracy assessment of the global TanDEM-X Digital Elevation Model with GPS data. *ISPRS J. Photogramm. Remote Sens.* **2018**, *139*, 171–182. [[CrossRef](#)]

48. Avtar, R.; Yunus, A.P.; Kraines, S.; Yamamuro, M. Evaluation of DEM generation based on Interferometric SAR using TanDEM-X data in Tokyo. *Physics and Chemistry of the Earth, Parts A/B/C*. **2015**, *83*, 166–177. [[CrossRef](#)]
49. Tachikawa, T.; Kaku, M.; Iwasaki, A.; Gesch, D.B.; Oimoen, M.J.; Zhang, Z.; Danielson, J.J.; Krieger, T.; Curtis, B.; Haase, J. *ASTER global digital elevation model version 2-summary of validation results*; NASA: Washington, DC, USA, 2011.
50. Gesch, D.; Oimoen, M.; Zhang, Z.; Danielson, J.; Meyer, D. Validation of the ASTER Global Digital Elevation Model (GDEM) Version 2 over the Conterminous United States. *Rep. to ASTER GDEM Version* **2011**, *2*, 281–286.
51. Santillan, J.R.; Makinano-Santillan, M. Vertical accuracy assessment of 30-m resolution alos, aster, and srtm global dems over northeastern mindanao, philippines. *Int. Arch. Photogramm. Remote Sens. Spat. Inf. Sci.* **2016**, *41*, 149–156. [[CrossRef](#)]
52. Rahman, M.S.; Di, L. The state of the art of spaceborne remote sensing in flood management. *Nat. Hazards* **2017**, *85*, 1223–1248. [[CrossRef](#)]
53. Takaku, J.; Tadono, T. PRISM geometric validation and DSM generation status. In Proceedings of the The First Joint PI Symposium of ALOS Data Nodes for ALOS Science Program, Kyoto, Japan, 19–23 November 2007.
54. Sekertekin, A.; Marangoz, A.M.; Akcin, H. Pixel-based classification analysis of land use land cover using Sentinel-2 and Landsat-8 data. *Int. Arch. Photogramm. Remote Sens. Spat. Inf. Sci.* **2017**, *42*, 91–93. [[CrossRef](#)]
55. Barsi, J.; Schott, J.; Hook, S.; Raqueno, N.; Markham, B.; Radocinski, R. Landsat-8 thermal infrared sensor (TIRS) vicarious radiometric calibration. *Remote Sens.* **2014**, *6*, 11607–11626. [[CrossRef](#)]
56. Yu, X.; Guo, X.; Wu, Z. Land surface temperature retrieval from Landsat 8 TIRS—Comparison between radiative transfer equation-based method, split window algorithm and single channel method. *Remote Sens.* **2014**, *6*, 9829–9852. [[CrossRef](#)]
57. Rajeshwari, A.; Mani, N.D. Estimation of land surface temperature of Dindigul district using Landsat 8 data. *Int. J. Res. Eng. Technol.* **2014**, *3*, 122–126.
58. Tahar, K.N. An evaluation on different number of ground control points in unmanned aerial vehicle photogrammetric block. *Int. Arch. Photogramm. Remote Sens. Spat. Inf. Sci.* **2013**, *40*, 93–98. [[CrossRef](#)]
59. Abdul-Rahman, A.; Zlatanova, S.; Coors, V. *Innovations in 3D geo information systems*; Springer Science & Business Media: Berlin, Heidelberg, 2007; ISBN 3540369988.
60. Courty, L.; Soriano-Monzalvo, J.C.; Pedrozo-Acuña, A. Evaluation of open-access global digital elevation models (AW3D30, SRTM and ASTER) for flood modelling purposes. *J. Flood Risk Manag.* **2019**, *12*, e12550. [[CrossRef](#)]
61. Apeh, O.I.; Uzodinma, V.N.; Ebinne, E.S.; Moka, E.C.; Onah, E.U. Accuracy Assessment of Alos W3d30, Aster Gdem and Srtm30 Dem: A Case Study of Nigeria, West Africa. *J. Geogr. Inf. Syst.* **2019**, *11*, 111–123. [[CrossRef](#)]
62. Akristiniy, V.A.; Boriskina, Y.I. Vertical cities—the new form of high-rise construction evolution. In *Proceedings of the E3S Web of Conferences*; EDP Sciences: Julius, France, 2018; Volume 33, p. 1041.
63. Özcan, A.H.; Ünsalan, C.; Reinartz, P. Ground filtering and DTM generation from DSM data using probabilistic voting and segmentation. *Int. J. Remote Sens.* **2018**, *39*, 2860–2883. [[CrossRef](#)]
64. Gevaert, C.M.; Persello, C.; Nex, F.; Vosselman, G. A deep learning approach to DTM extraction from imagery using rule-based training labels. *ISPRS J. Photogramm. Remote Sens.* **2018**, *142*, 106–123. [[CrossRef](#)]
65. Xiaogang, N.; Qin, Y.; Yang, B. Extracting and analyzing urban built-up area based on impervious surface and gravity model. In Proceedings of the Joint Urban Remote Sensing Event 2013; IEEE, Sao Paulo, Brazil, 21–23 April 2013.
66. Phiri, D.; Morgenroth, J. Developments in Landsat land cover classification methods: A review. *Remote Sens.* **2017**, *9*, 967. [[CrossRef](#)]
67. Cortes, C.; Vapnik, V. Support-vector networks. *Mach. Learn.* **1995**, *20*, 273–297. [[CrossRef](#)]
68. Shao, Y.; Lunetta, R.S. Comparison of support vector machine, neural network, and CART algorithms for the land-cover classification using limited training data points. *ISPRS J. Photogramm. Remote Sens.* **2012**, *70*, 78–87. [[CrossRef](#)]
69. Zhang, T.; Tang, H. A Comprehensive evaluation of approaches for built-up area extraction from Landsat OLI images using massive samples. *Remote Sens.* **2019**, *11*. [[CrossRef](#)]

70. Li, Z.-L.; Tang, B.-H.; Wu, H.; Ren, H.; Yan, G.; Wan, Z.; Trigo, I.F.; Sobrino, J.A. Satellite-derived land surface temperature: Current status and perspectives. *Remote Sens. Environ.* **2013**, *131*, 14–37. [[CrossRef](#)]
71. Kahle, A.B.; Morrison, A.D.; Tsu, H.; Yamaguchi, Y. Geologic remote sensing in the thermal infrared. In Proceedings of the New technology for geosciences: proceedings of the 30th International Geological Congress, Beijing, China, 4–14 August 1996.
72. Morshed, N.; Yorke, C.; Zhang, Q. Urban expansion pattern and land use dynamics in Dhaka, 1989–2014. *Prof. Geogr.* **2017**, *69*, 396–411. [[CrossRef](#)]
73. Singh, R.; Grover, A.; Zhan, J. Inter-seasonal variations of surface temperature in the urbanized environment of Delhi using Landsat thermal data. *Energies* **2014**, *7*, 1811–1828. [[CrossRef](#)]
74. Gallo, K.; Hale, R.; Tarpley, D.; Yu, Y. Evaluation of the relationship between air and land surface temperature under clear- and cloudy-sky conditions. *J. Appl. Meteorol. Clim.* **2011**, *50*, 767–775. [[CrossRef](#)]
75. Guo, G.; Zhou, X.; Wu, Z.; Xiao, R.; Chen, Y. Characterizing the impact of urban morphology heterogeneity on land surface temperature in Guangzhou, China. *Environ. Model. Softw.* **2016**, *84*, 427–439. [[CrossRef](#)]
76. Guo, G.; Wu, Z.; Xiao, R.; Chen, Y.; Liu, X.; Zhang, X. Impacts of urban biophysical composition on land surface temperature in urban heat island clusters. *Landsc. Urban Plan.* **2015**, *135*, 1–10. [[CrossRef](#)]
77. Ruffieux, D.; Wolfe, D.E.; Russell, C. The effect of building shadows on the vertical temperature structure of the lower atmosphere in downtown Denver. *J. Appl. Meteorol.* **1990**, *29*, 1221–1231. [[CrossRef](#)]
78. Zheng, Z.; Zhou, W.; Yan, J.; Qian, Y.; Wang, J.; Li, W. The higher, the cooler? Effects of building height on land surface temperatures in residential areas of Beijing. *Phys. Chem. Earth Parts A/B/C* **2019**, *110*, 149–156. [[CrossRef](#)]
79. Peng, F.; Gong, J.; Wang, L.; Wu, H.; Yang, J. Impact of building heights on 3d urban density estimation from spaceborne stereo imagery. *Int. Arch. Photogramm. Remote Sens. Spat. Inf. Sci. - ISPRS Arch.* **2016**, *41*, 677–683. [[CrossRef](#)]
80. Misra, P.; Avtar, R.; Takeuchi, W. Comparison of Digital Building Height Models Extracted from AW3D, TanDEM-X, ASTER, and SRTM Digital Surface Models over Yangon City. *Remote Sens.* **2018**, *10*, 2008. [[CrossRef](#)]
81. Cai, M.; Ren, C.; Xu, Y.; Lau, K.K.L.; Wang, R. Investigating the relationship between local climate zone and land surface temperature using an improved WUDAPT methodology—A case study of Yangtze River Delta, China. *Urban Clim.* **2018**, *24*, 485–502. [[CrossRef](#)]
82. Wang, R.; Cai, M.; Ren, C.; Bechtel, B.; Xu, Y.; Ng, E. Detecting multi-temporal land cover change and land surface temperature in Pearl River Delta by adopting local climate zone. *Urban Clim.* **2019**, *28*, 100455. [[CrossRef](#)]
83. Chen, F.; Yang, S.; Yin, K.; Chan, P. Challenges to quantitative applications of Landsat observations for the urban thermal environment. *J. Environ. Sci.* **2017**, *59*, 80–88. [[CrossRef](#)] [[PubMed](#)]
84. Xu, H. Analysis of impervious surface and its impact on urban heat environment using the normalized difference impervious surface index (NDISI). *Photogramm. Eng. Remote Sens.* **2010**, *76*, 557–565. [[CrossRef](#)]
85. Yang, J.; Wong, M.-S.; Ho, H.C. Retrieval of Urban Surface Temperature Using Remote Sensing Satellite Imagery. In *Big Data for Remote Sensing: Visualization, Analysis and Interpretation*; Springer: Basel, Switzerland, 2018.

